Modeling the afferent dynamics of the baroreflex control system

Adam Mahdi[1], Jacob Sturdy[1], Johnny T. Ottesen[2], Mette S. Olufsen[1,*]
1 Department of Mathematics, North Carolina State University, Raleigh, NC, USA
2 Department of Science, Systems, and Models, Roskilde University, Roskilde, Denmark
∗ **E-mail: msolufse@ncsu.edu**

Abstract

In this study we develop a modeling framework for predicting baroreceptor firing rate as a function of blood pressure. We test models within this framework both quantitatively and qualitatively using data from rats. The models contain three parts reflecting the mechanisms engaged to activate baroreflex regulation including: arterial wall deformation, stimulation of mechanoreceptors located in the BR nerve-endings, and modulation of the action potential frequency. The three sub-systems are modeled individually following well-established biological principles. The first sub-model, predicting arterial wall deformation, uses blood pressure as an input and outputs circumferential strain. The mechanoreceptor stimulation model, uses circumferential strain as an input, predicting receptor deformation as an output. Finally, the neural model takes receptor deformation as an input predicting the BR firing rate as an output. Our results show that nonlinear deformation of the arterial wall is essential to account for increased stiffening with increased pressure. This was observed when testing the models using multiple experiments with a single set of parameters. We find that to model the response to a square pressure stimulus, giving rise to post-excitatory depression, it is necessary to include an integrate-and-fire model, which allows the firing rate to cease when the stimulus falls below a given threshold. We show that our modeling framework in combination with sensitivity analysis and parameter estimation can be used to test and compare models. Finally, we demonstrate that our preferred model can exhibit all known dynamics and that it is advantageous to combine qualitative and quantitative analysis methods.

Author Summary

Many people have experienced lightheadedness when standing up, yet the exact cause of this phenomenon remains unknown. For some people, lightheadedness occurs because of anomalies in the blood pressure control (the *baroreflex*) system, which keeps blood flow and pressure at homeostasis. One way to explore this system is via mathematical modeling, which can offer valuable insights into the complex dynamic processes. This study develops a framework for modeling activity of the baroreceptor neurons. The models consist of three components reflecting three physiological mechanisms relating blood pressure to the baroreceptor firing rate: modulation of arterial blood pressure causes dilation of the arterial wall, stimulating mechanoreceptors within the baroreceptor nerve endings, emanating from the aortic arch and carotid sinus, which in turn modulates the firing rate of the baroreceptor neurons. This signal is integrated in the brain stem, stimulating baroreflex efferents to counteract the pressure increase. In this study, we review the main static and dynamic features of the baroreceptor firing activity, and show, using a combination of modeling techniques and rat aortic baroreceptor data, how to build a computationally efficient, yet biologically correct model. These models are important components for eventually predicting efferent responses, such as: heart rate, contractility or stroke volume.

Introduction

The main role of the cardiovascular (CV) system is to provide adequate oxygenation of all tissues, a function which is achieved by maintaining homeostasis of blood flow and pressure. When a mammal is subjected to an orthostatic maneuver (e.g., running, jumping, etc.), its blood volume is redistributed,

moving the system state away from homeostasis [1]. To re-establish homeostasis a number of control mechanisms are activated regulating vascular resistance and compliance, and pumping efficiency and frequency. An important contributor to this control system is the *baroreflex*, which uses specialized neurons called baroreceptors (BR) for signaling [2]. The BR neurons emanate in the arterial wall and terminate in the nucleus solitary tract, where sensory information is integrated. These neurons are continuously stimulated via activation/inhibition of mechanosensitive receptors responding to changes in arterial wall stretch imposed by pulsating blood pressure [3]. This stimulus modulates the formation of action potentials propagating along the BR nerves terminating in the NTS, where efferent signals are generated to regulate heart rate, cardiac contractility, and vascular resistance and compliance. It is known that the baroreflex system contributes to short-term blood pressure regulation, operating on a time-scale of seconds to minutes [4]. For example upon head-up tilt, blood is pooled in the lower extremities, increasing blood pressure in the lower body, while decreasing it in the upper body, causing an imbalance, which persists until the baroreflex system is activated. Figure 1 shows a schematic representation of the baroreflex pathways. While the BR pathways are generally well established, analysis of the complete control system, including afferent and efferent signaling, is hindered by the difficulty of measuring the activity of each component without disrupting the feedback loop. For example, in-vivo, only macroscopic quantities can be measured non-invasively including heart rate and blood pressure. From such measurements it is difficult to examine how the individual components of the system interact and consequently it is difficult to determine which sub-systems are compromised for subjects experiences baroreflex failure [5] or decreased arterial baroreflex sensitivity [6]. These difficulties limits the development of targeted diagnosis procedures and treatment plans aiming to alleviate symptoms for patients.

Mathematical modeling is an eminent tool for gaining more insight into this complex feedback loop, offering a stringent and systematic way to identify underlying mechanisms of the system. For example, the only way to estimate model parameters and thereby predict essential biomarkers, that may not be directly measurable, is by using models in combination with direct measurements. Modeling also offers a way to understand complex systems, as it make the inaccessible accessible, a concept denoted the "mathematical microscope" [7].

This paper will focus solely on the afferent part of the baroreflex system, while future studies will address efferent signaling and integration of the two parts within a system level model. Since the 1950s researchers have put forward numerous mathematical models [8–19], which tried to integrate known dynamics with hypothesized mechanisms in order to provide more understanding of the system as a whole. Many insights have been gained, however, most of these models were developed to describe BR response to a particular stimulus, rather than to a range of stimuli eliciting all known responses. Therefore they all lead to different hypothesis explaining the system mechanisms. Inspired by shortcomings of previous studies, we developed a *modeling framework* containing model components reflecting physiological pathways. This framework splits the afferent signaling into three parts predicting vessel wall deformation, mechanoreceptor stimulation, and the frequency of action potential generation. For each component we propose multiple models, which we test both qualitatively and quantitatively. This new approach allows us to understand the contribution of each component model to the overall signal. For example, if the objective is to build a BR model that can reflect the response to a sinusoidal pressure stimulus observed experimentally, the modeling framework can be used to identify which combinations of components are sufficient to describe the experimental outcome, and which component models may be excluded from possible explanations of observed features. Moreover, we show how our framework may be used to inform hypotheses, by suggesting a particular component mechanism responsible for generating a given pressure-response feature of BR firing.

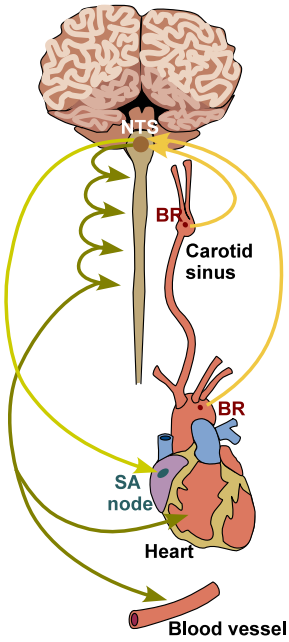

Figure 1. Schematic representation of the BR feedback system. Stretch sensitive BR neurons emanate in the carotid sinuses and the aortic arch. In these arteries, dynamic changes in blood pressure cause vessel deformation, modulating stretch of mechanoreceptors channels found in the BR nerve endings. Stimulation of these receptors modulates frequency of action potential formation, a signal integrated in the NTS. From the NTS, efferent sympathetic and parasympathetic outputs are generated determining the concentrations of neurotransmitters acetylcholine and noradrenaline, which stimulate or inhibit heart rate, cardiac contractility, vascular resistance and compliance, the latter via activation of smooth muscle cells constricting or dilating the radius of arteriolar vessels.

Methods

Experimental data and its features

In this section we describe the main *qualitative* characteristics of BR firing rate as well as the data used for *quantitative* model tests.

Qualitative features of the BR firing rate

Although BR firing patterns depend on the type of BR, e.g., whether they are connected to myelinated or unmyelinated axons [20], there are a number of features nearly all BR neurons exhibit. We characterize these according to observations obtained by stimulating isolated rat aortic BR neurons with a range of pressure stimulus including: sinusoidal, step increases and decreases, and ramp increases and decreases (Figure 2). The most common features of the BR response to imposed pressure stimuli include: saturation and threshold (Figure 10), adaptation and overshoot (Figures 7-10), as well as post-excitatory depression and rectification (Figure 10). Below, we describe each of these firing rate patterns in more detail.

Threshold. Observed in response to a step or ramp increase in pressure (Figure 2b,d). This phenomenon was first described by Bronk and Stella [21, 22] in the 1930s. They observed that a small step increase from a given baseline blood pressure did not trigger BR firing, but when the pressure was

increased above a certain threshold, the BR nerve began to fire continuously. The threshold was later observed to increase with an increased baseline pressure [23–26]. Moreover, Seagard et al. [27] observed that the type of baroreceptor (myelinated or unmyelinated) strongly affects the threshold pressure. The precise mechanisms underlying the threshold phenomena remains unknown, but it is thought to be attributed to the characteristics of ion channels associated with generation of action potentials [28].

Saturation. Observed in response to a ramped increase of blood pressure (Figure 2d). As the pressure is increased linearly, the BR firing rate first increases almost linearly (with pressure). Then, at a given frequency, the firing rate approaches some limiting value (the saturation level) [23] (Figure 10). This phenomenon was also observed by Bronk and Stella [21, 22]. They noted that for normotensive rabbits, the firing rate saturates around 120-140 Hz. Later, Seagard et al. [27] studied saturation by stimulating a single carotid BR nerve fiber, extracted from a mongrel dog, with a slow linearly increasing pressure. This experiment showed firing rate saturation at 46.5 ± 2.5 Hz. These observations led to the separation of nerves as type I (large myelinated aortic (A) nerve fibers) and type II (smaller aortic (A) and unmyelinated carotid (C) nerve fibers). They observed type I BR neurons displayed a discontinuous firing pattern, characterized by a sudden onset of discharge at the average threshold pressure of 73.3 ± 5.2 mmHg, whereas type II neurons displayed a continuous, sigmoidal firing pattern saturating at 19.2 ± 2.1 mmHg.

Adaptation. Observed in response to a step change in pressure (Figure 2b). In response to this stimulus, the firing rate adapts to a new level depending on the magnitude of the pressure change (Figures 7-10). This phenomenon was first observed by Landgren [8, p.7], who discovered that 50% of adaptation occurs within 0.1 (sec) following the the pressure stimulus, 95% is completed after 30 sec, whereas full adaptation requires a very long time, more than 2 minutes. It was later confirmed by Srinivasen and Nudelman [11] and Brown et al. [29], though from these later studies it is not clear that adaptation requires three distinct timescales. Moreover, Brown [29] noted that the frequency of the adapted firing rate is the same whether the baseline pressure level is reached from a higher or a lower pressure level. Several studies have observed that the level of the steady-discharge is proportional to the applied pressure [20, 30]. No mechanism has been established as the cause of adaptation; however, Franz et al. [31, p.823] propose viscoelastic relaxation as the source of adaptation in the firing rate.

Overshoot. Observed following either a step [31] or a ramp increase of pressure [10] (Figure 2d). The firing rate responds by immediately increasing the rate of discharge, followed by a slow adaptation to a new lower steady state value (Figures 7-10). Brown et al. [30, Figure 5] noted that the relationship between the size of the overshoot and the level of the pressure stimulus is almost linear. It is the BR response immediately following the onset of the pressure stimulus that is referred to as overshoot, thus overshoot is always followed by adaptation (explained above), and therefore mechanisms giving rise to overshoot are closely related to the ones associated with adaptation.

Post-excitatory depression (PED). Observed following a step-decrease in pressure (Figure 2c). In response to this stimulus the BR firing ceases for a short period, after which it recovers to a rate corresponding to the newly established pressure level (Figure 8). While the term PED was put forward by Brown et al. [29, 32], who studied the phenomena extensively, the phenomenon was first observed by Bronk and Stella [21] when they noticed that BR firing ceased during diastole. Later, Wan et al. [33] observed that the length of the pause depends on the depth of the pressure drop. Brown [32, p.504], suggested that an electrogenic-sodium pump could be the potential mechanism for this phenomena.

Asymmetry (or hysteresis). Observed following a sequential rise and fall of blood pressure (see sinusoidal, square, and triangular stimulus shown in Figure 2). This phenomenon was described by Katona and Barnett [34], but have also been discussed by Coleridge, Angell, Pelletier et al. [23, 35–37]. These studies all explained the phenomenon from observing that the BR firing rate exhibits asymmetrical responses to rising and falling blood pressure (Figure 10). However, asymmetry can be observed in response to any stimuli involving a symmetric increase and decrease in pressure. Thus it may also be observed in PED (Figure 8) and in response to periodic sinusoidal forcing (Figures 6a and 10). In the time-domain, it may not be easy to see that a sinusoidal stimulation leads to asymmetry, but it can be observed by

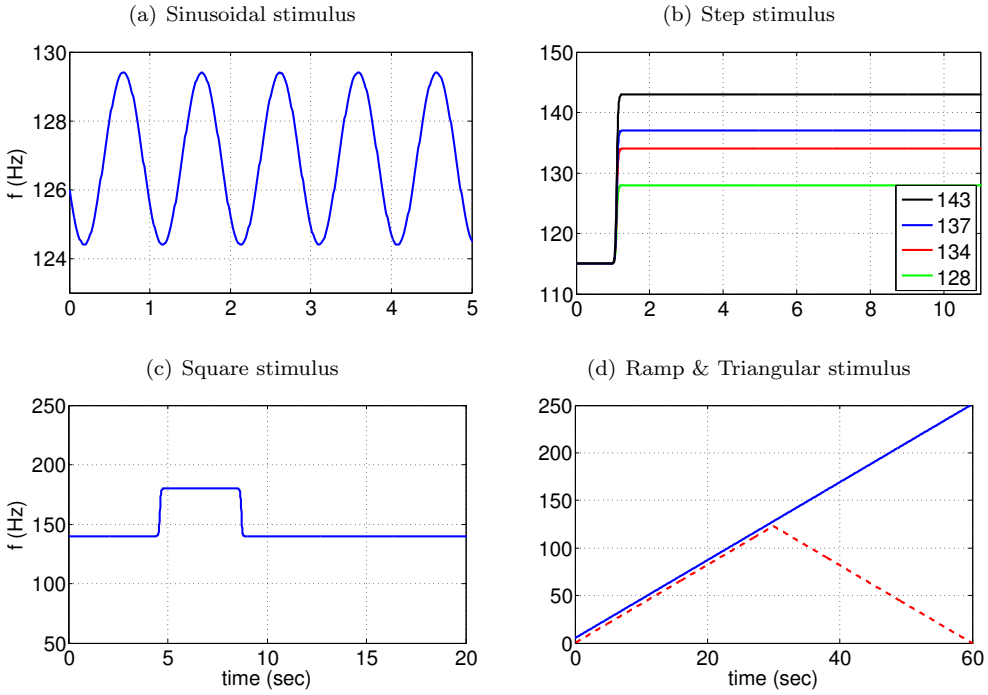

Figure 2. Various types of BR input pressure. To test our models we applied a number of pressure stimuli: (a) sinusoidal, (b) step increases, (c) square (step increase followed by a step decrease), (d) ramp and triangular. All stimuli were used for qualitative model predictions, while quantitative simulations were only done using stimuli shown in (a-c).

depicting BR firing as a function of pressure, which gives rise to hysteresis loops (Figure 6b). This phenomenon is closely related to adaptation and overshoot, thus viscoelastic relaxation exhibited by the arterial wall, could explain its origin.

Description of experimental data

So far we have focused on describing the qualitative features of the BR firing rate. However, if the objective is to understand how these responses are modulated in disease or between species it may be important to predict the BR firing rate quantitatively.

Below we describe the main features of data used for quantitative predictions. All quantitative data were obtained by digitizing results reported by Brown et al. [20] and Saum et al. [32]. From these studies we extracted data from a total of six experiments, grouped with respect to the applied pressure stimulus: sinusoidal, step increase with four different amplitudes, and a square pulse. These stimuli are depicted in Figure 2a-c.

Sinusoidal pressure stimulus. To test the models' abilities to mimic *in vivo* dynamics, we used data reported by Brown et al. [20, Figure 2A]. They stimulated the stretch-sensitive receptors using a sinusoidal pressure stimulus mimicking the natural blood pressure rhythm and recorded the corresponding BR firing rate. Several studies [9, 17, 38–40] have reported similar experiments. This type of data allows us to evaluate whether the model can predict asymmetry (Figure 6) and rectification (Figure 10). The study [20] reports firing rate responses recorded from 11 experiments using myelinated aortic BR axons extracted from Wistar-Lewis strain normotensive rats aged 4-6 months. For each experiment the neuron

was stimulated using sinusoidal pressure wave with a frequency of 20 Hz, an amplitude of 5 mmHg, and a mean pressure of 127 mmHg. Steadily oscillating pressures were recorded over a period of 5 seconds. More details about experimental preparation can be found in [30,32]. To obtain a smooth input stimulus, we fit the data to a sinusoidal function of the form

$$p(t) = p_0 + 2.5\sin(p_2 - p_1 t), \tag{1}$$

where $p_0 = 127$ mmHg. We estimated parameters p_1 and p_2 using the initial values $p_1 = 6.45$ and $p_2 = 46.75$. Resulting parameters are given in Table 4.

Multistep pressure stimulus. To predict overshoot followed by adaptation, we digitized BR firing rate data reported in [20, Figure 5]. This study shows BR discharge in response to four pressure step increases from a baseline pressure of 115 mmHg. The four step-increase stimuli are: 13 (to 128), 19 (to 134), 22 (to 137), and 28 (to 143) mmHg (Figure 2b). Experiments were done over a period of 12 sec, allowing the BR firing rate to adapt to a new steady level of discharge. In this study we used data reported by Brown et al. [20], though several experimental studies have reported similar observations [30, 41]. It should be noted, that no graph depicted the pressure stimulus. Brown et al. [20] reported the baseline pressure as well as the level of the pressure increase, but not the exact time denoting the onset of the stimulus. We modeled the stimulus using a smooth function of the form

$$p(t) = \frac{p_{up}(t^{\kappa_u} + \delta_u^{\kappa_u})}{t^{\kappa_u} + (p_{up}/p_{dow})\delta_u^{\kappa_u}}, \tag{2}$$

where p_{dow}, p_{up} denote the baseline pressure and the increased pressure, respectively; δ_u denotes the onset of the pressure step increase, and κ_u denotes the steepness of the increase. For the dataset under consideration the values $p_{dow} = 115$, and $p_{up} = \{128, 134, 137, 143\}$ were taken from [20], while we estimated δ_u and κ_u. Initial values for these parameters were set to $\delta_u = 1.1$ and $\kappa_u = 10$ approximating the onset described in the experiment [20, Figure 5]. Optimized parameter values along with p_{dow} and p_{up} are given in Table 4.

Square pressure pulse stimulus. To predict PED, we digitized data reported in Saum et al. [32, Figure 1], which examined PED and adaptation in slowly adapting aortic BR neurons extracted from normotensive and spontaneously hypertensive rats. Though this phenomenon has also been reported in several other studies including [8, 31–33, 42]. The study by Saum et al. [32] stated that PED could be elicited either mechanically by employing single or double pressure steps, or electrically by stimulating myelinated aortic BR axons extracted from normotensive Wistar-Lewis rats aged 4-6 month. The data used shows a steady state discharge was elicited by stimulating the nerve with a baseline pressure of 140 mmHg. After 4 sec the pressure was increased by 40 mmHg to 180 mmHg for a period of 4 sec, after which it was reset to the baseline pressure of 140 mmHg. To allow the neuron to fully recover following the pressure drop, data were recorded over a period of 20 sec (Figure 8). In order to avoid the problem of non-differentiability we modeled the pressure stimulus using the smooth function

$$p(t) = p_b + p_{up}\tanh(\kappa(t - \delta_u))/2 - p_{dow}\tanh(\kappa(t - \delta_d))/2, \tag{3}$$

where tanh is the hyperbolic tangent. For this stimulus we used $p_b = 140$, $p_{up} = 40$, $p_{dow} = 40$, $\kappa_u = 20$. Other parameters were optimized and are reported in Table 6.

Models

To model the dynamics, which produce the BR firing rate in response to given blood pressure stimuli, we include three components separating distinct physiological pathways, and for each component we develop a number of linear and nonlinear models. The three components (Figure 3) include: arterial wall deformation, mechanoreceptor stimulation, and action potential generation. As a driving force for

Figure 3. Block diagram used to predict BR firing in response to an applied blood pressure stimulus. Applied changes in blood pressure induce changes in the arterial wall strain, which induce changes sensed by stretch sensitive mechanoreceptors found in BR within the arterial wall. This stimulus modulates frequency of action potential formation, which can be used to predict BR firing rate.

the models we use arterial pressure, which determines arterial wall deformation quantified by the wall strain. The wall deformation, stimulates the stretch sensitive mechanoreceptors found in the BR nerve endings within the arterial wall. Thus changes in blood pressure modulate the opening of these channels, and thereby the current flowing through them, which determine the rate at which action potentials are formed. The time between subsequent action potentials determines the firing rate, and thus our models relate the receptor strain to the frequency of action potentials, thereby allowing us to predict the BR firing rate. For each model component, described below, we review previous modeling methodologies and use these to inform the design of the new component models, collectively used to describe the firing rate of afferent BR neurons in response to an applied blood pressure stimulus.

Arterial wall deformation

BR nerves emanate in the wall of the the aortic arch and the carotid sinus and terminate in the NTS [43]. Action potentials transmitted along these nerves are generated by stimulation of mechanoreceptors found in the wall. These nerves are stimulated by pressure pulses passing through the vessel, and their firing patterns are modulated in response to changes of the frequency and magnitude of the pressure stimulus. It is well known [44] that the arterial wall deforms viscoelasticily, though little is known about how this deformation impacts stimulation of the mechanoreceptors. This section describes models predicting vessel strain as a function of blood pressure, while the next section describes characterization of mechanoreceptor stretch, which in turn modulates BR firing rate.

The arterial wall is composed of three layers: *tunica intima*, the inner most layer; *tunica media*, the middle layer, and *tunica adventitia*, the outer layer [45]. The arterial wall which is 70% water also consists of muscle fibers, elastin, collagen, and ground substance. Smooth muscle cells are found in the walls of most blood vessels, particularly in the tunica media layer. As a vessel contracts and expands under neural control, not only does the vessel's radius change, so do its elastic properties. The protein elastin, which is especially abundant in larger blood vessels, such as the aorta, exhibits nonlinear elastic response to an applied stimulus, which allows the vessel to recover to its relaxed state after an imposed stimulus. Collagen, another protein is present in all vessels, although the amount of collagen in smaller vessels is significantly larger than in the aorta [46]. This fibrous structural protein forms tough bundles, which support the vessel wall and give cells external structure; it has great tensile strength [47, 48]. It is this protein which accounts for viscoelastic creep during arterial wall deformation.

Detailed prediction of arterial wall strain requires complex, anisotropic, viscoelastic models, accounting for dynamics associated with each layer of the wall as well as the interaction between the layers [44]. While such models can provide detailed description of wall deformation, they cannot easily be integrated with a higher-level model predicting BR firing rate. Another class of models are those assuming that the arterial wall is isotropic. Such models can be represented by a thin shell, and since arteries are tethered in the longitudinal direction, viscoelastic deformation is dominantly in the circumferential direction (cf. [49]). Such models predict the cross-sectional strain of the arterial wall in response to induced changes in applied stress, corresponding to the blood pressure [46]. Again, depending on the fidelity

needed, these "stress-strain" models can be simplified. The simplest stress-strain models ignore viscous deformation and treat the wall as purely elastic. Such models may use either a linear or nonlinear relation between stress and strain. In this study we consider three wall models, of which one is linear and elastic (W_e, subscript e for elastic), one is linear and viscoelastic (W_{ve}, subscript ve for viscoelastic), and one is nonlinear and elastic (W_{ne}, subscript n for nonlinear and e for elastic).

Table 1. Elastic and viscoelastic models of arterial wall strain.

Model	**Elastic response** $s^e[\cdot]$	**Creep** $K(\cdot)$	**Type**
W_e	$\frac{r_0}{Eh}p$	1	elastic
W_{ve}	$\frac{r_0}{Eh}p$	$1 - A_1 e^{-t/b_1}$	viscoelastic
W_{ne}	$1 - \frac{A_0(\alpha^k + p^k)}{A_0\alpha^k + A_m p^k}$	1	nonlinear elastic

The unified QLV formulation in (8) encompasses all models studied here. The first column lists the model, the second the elastic response, the third the creep, and the fourth states if the model is linear or nonlinear.

Linear elastic wall model (W_e). For a thin walled elastic vessel with an isotropic wall, vessel-wall deformation can be predicted using *Laplace's law* relating circumferential strain $\sigma_{\theta\theta}$ to blood pressure p as

$$\sigma_{\theta\theta} = \frac{pr}{h},$$

where r denotes the radius of the vessel, h the wall thickness. The circumferential strain $\epsilon_{\theta\theta}$ is defined as

$$\epsilon_{\theta\theta} = \frac{r - r_0}{r_0},$$

where r_0 is the unstressed radius at zero pressure. For a thin-walled elastic vessel, the circumferential stress and strain can be related by

$$\epsilon_{\theta\theta} = \frac{\sigma_{\theta\theta} - \nu\sigma_{rr} - \nu\sigma_{zz}}{E},$$

where σ_{rr}, σ_{zz} , ν, and E denote the normal stress in the radial direction, the normal stress in the longitudinal direction, the Poisson's ratio, and Young's modulus. Since we neglect the deformation in the axial direction we obtain the simplified relationship

$$\epsilon_{\theta\theta} = \frac{\sigma_{\theta\theta}}{E}.$$

Now substituting previously obtained expressions for $\epsilon_{\theta\theta}$ and $\sigma_{\theta\theta}$ we get

$$\frac{r - r_0}{r_0} = \frac{pr}{Eh}.$$

Equivalently

$$\epsilon_w = \frac{r - r_0}{r} = k_{wall}\, p, \qquad k_{wall} = \frac{r_0}{Eh}. \tag{4}$$

The quantity ϵ_w is a relative measure of the circumferential wall strain and can be modeled in light of Hooke's law as a linear spring.

Nonlinear elastic wall model (W_{ne}). It is well known that the area-pressure response curve is nonlinear and can be modeled using a sigmoidal function, accounting for saturation of the vessel wall deformation at both high and low pressures. Following [46, 50] the pressure-area relationship can be modeled as

$$A(p) = (A_m - A_0)\frac{p^k}{\alpha^k + p^k} + A_0,$$

where A_0 and A_m are the unstressed and maximum cross-sectional area; α is the characteristic pressure at which the vessel starts to saturate; and k determines the steepness of rise of the sigmoidal curve, representing the stiffness in the lumen distention due to changes in pressure. Using (4) as a definition of wall strain ϵ_w, we obtain

$$\epsilon_w = 1 - \sqrt{\frac{A_0(\alpha^k + p^k)}{A_0\alpha^k + A_m p^k}}. \tag{5}$$

Viscoelastic wall models (W_{ve}). While the main contribution to arterial wall deformation is elastic, as mentioned above, the arterial wall is composed of tissue that has viscoelastic properties. Viscoelastic models encompass both elastic deformation and viscoelastic creep, and thus can be described using either linear or nonlinear elastic responses.

Linear viscoelastic response of the arterial wall is typically, although not solely, described using a number of springs (elastic elements) and dashpots (viscous elements) in various configurations. The so-called standard linear solid (SLS), is one of the most commonly used examples of such configurations. It involves a Maxwell element (spring E_1 and dashpot η_1 in series) in parallel with a spring E_0. It is easy to establish that the total stress-strain relationship given by the following constitutive equation

$$\epsilon + \tau_a \frac{d\epsilon}{dt} = \frac{1}{E_0}\Big(\sigma + \tau_b \frac{d\sigma}{dt}\Big), \qquad \tau_a = \frac{\eta_1}{E_0}\Big(1 + \frac{E_0}{E_1}\Big), \qquad \tau_b = \frac{\eta_1}{E_1}. \tag{6}$$

To apply the SLS model to the arterial wall, we think of ϵ as vessel distention ϵ_w and the stress σ as the blood pressure p. Moreover, assuming the arterial wall is a thin-walled elastic tube we can substitute $E_0 = Eh/r_0$ and obtain the following equation

$$\epsilon_w + \tau_a \frac{d\epsilon_w}{dt} = k_{wall}\Big(p + \tau_b \frac{dp}{dt}\Big), \qquad k_{wall} = \frac{r_0}{Eh}.$$

In order to avoid numerical differentiation of the data, following [46] we apply the integrating factor and transform this equation to

$$\epsilon_w = \left(\epsilon_w(t_0) - \frac{k_{wall}\,\tau_b}{\tau_a}p(t_0)\right) e^{-\frac{t-t_0}{\tau_a}} + \frac{k_{wall}\,\tau_b}{\tau_a}p(t) + k_{wall}\frac{\tau_a - \tau_b}{\tau_b^2}\int_{t_0}^{t} e^{-\frac{t-\gamma}{\tau_a}}p(\gamma)\,d\gamma. \tag{7}$$

QLV framework. Formulated as linear elements in series and parallel, the above model cannot directly be extended to account for nonlinear elastic response; moreover, it is limited to models described using a finite number of components. It was noted by Fung [49], that biological tissues are not elastic and that strain history affects the stress. Moreover, there is a difference in the stress response between loading and unloading. Generalizing linear viscoelastic theory, Fung [49], introduced the so-called quasi-linear viscoelastic theory (QLV), which has been used successfully to model stress-strain relationships involving living tissues [51, 52]. The QLV theory is a flexible framework that includes linear viscoelastic theory and provides a more accurate description of the pressure-strain curve, especially in living tissues. We proceed with the assumption that the arterial wall can be modeled as homogeneous and isotropic thin walled cylindrical vessel [53]. Therefore the wall strain as a function of pressure can be determined as

$$\epsilon_w = \int_{\infty}^{t} K(t-\gamma)\frac{\partial s^e[p(\gamma)]}{\partial \gamma}d\gamma, \tag{8}$$

where $K(t)$ is a creep function, and $s^e[p(\gamma)]$ is the elastic response [46, 49]. Finally, it should be noted that all the linear and nonlinear arterial wall models described above can be expressed within the unified framework of the QLV theory, see Table 1.

Mechanoreceptor stimulation

The BR nerves emanating in the adventitial layer of the aortic arch and carotid arteries form a complex branching network [54]. In rats electron microscopy studies have revealed that BR aortic nerve fibers form bundles, usually containing one myelinated and five unmyelinated fibers of different sizes [54, p.401]. Each bundle is surrounded by a protective sheath, perineurium. Both unmyelinated and myelinated fibers are sheathed in Schwann cells and are embedded in collagen, see [54, p.404] and [55, 56]. Because these nerve endings are embedded in the arterial wall, deformations of the arterial wall also deform the nerve endings. This deformation stimulates stretch sensitive, non-selective cation channels that serve to transduce the changes in the nerve ending structure into an electrical signal, which is encoded into the firing pattern of the BR neuron [2].

We propose a model specifying the strain effected specifically at the nerve endings as a result of a given arterial wall strain. Thus our model seeks to capture the stimulation of the mechanoreceptive nerve endings by capturing the stretching dynamics of the nerve endings as the arterial wall expands or contracts in response to changes in pressure. We propose models with the assumption that viscoelastic properties of BR nerve ending connective tissue are the key factor in the transduction process [57, 58]. Following the ideas used in previous BR modeling studies [13, 59]; and before in the modeling of the muscle spindle dynamics [60, 61] we describe the coupling of the strain sensed by the mechanoreceptors to the wall deformation using n Voigt bodies in series with a spring (Figure 4). Following this idea, the strain sensed by the mechanoreceptors in response to the arterial wall deformation is given by

$$\epsilon_{ne} = \epsilon_w - \epsilon_1, \tag{9}$$

where ϵ_w denotes the strain of the wall, and ϵ_1 denotes the strain of the first Voigt body. Choosing the parameters a_{ij} and $b_1, \ldots, b_n$, determined by the spring, E, and dashpot, η, constants, the model given in Figure 4 can be described using the dynamical system

$$\frac{d\epsilon_j}{dt} = a_{j1}\epsilon_1 + \ldots + a_{jn}\epsilon_n + b_j\epsilon_w \qquad j = 1, 2, \ldots, n$$

where $\epsilon_j, (j = 1, \ldots, n)$ is the relative displacement within each Voigt body. Consequently, our model assumes a declining afferent sensory activity during constant intensity stimulation, a fundamental property of mechanoreceptors that can be described in terms of viscoelastic relaxation processes in the vessel wall [31, 62]. Below we describe, in more detail, the computational aspects of this element of the BR model, analyzing model components including one, two, and three Voigt bodies. Since the strain is predicted by Voigt bodies, we have denoted this model component V_i where $i = 1, 2, 3$ denotes the number of Voigt bodies included.

One Voigt body model (V_1). We start with the simplest Voigt body model. This consists of one Voigt body in series with a spring (Figure 4 for $n = 1$). The governing equation predicting the nerve ending deformation is given by

$$\frac{d\epsilon_1}{dt} = -(\alpha_1 + \beta_1)\epsilon_1 + \alpha_1\epsilon_w, \tag{10}$$

where β_1 and α_1 depend on the spring constants E_{ne}, E_1 and viscous element η_1 as stated in Table 3. Since equation (10) is a first-order linear ODE, the total strain sensed by the mechanoreceptor is equivalent to the strain on the Voigt body, thus this model component only exhibit one time-scale τ_{v_1} associated with the strain ϵ_w. This time-scale is given by

$$\tau_{v_1} = \alpha_1 + \beta_1. \tag{11}$$

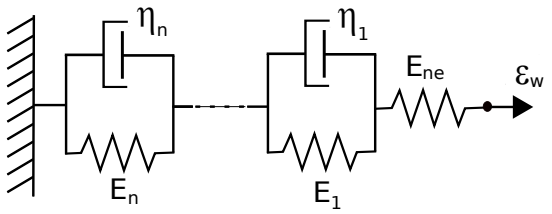

Figure 4. A schematic illustration of the strain sensed by the mechanoreceptors. The spring and n Voigt bodies (a parallel spring and dashpot) in series shown here predicts the strain sensed by the mechanoreceptors relative to the deformation of the arterial wall. The spring E_{ne} represents the elasticity of the BR nerve endings, whereas the n Voigt bodies reflect the viscoelastic properties of the surrounding connective tissue. Each element n provides a timescale adaptation of BRs firing rate in response to a step increase in pressure observed in experiments. This study compares the cases $n = 1, 2, 3$.

Two Voigt body model (V_2). The model with two Voigt bodies and a spring in series (Figure 4 for $n = 2$) can be described by the following system of differential equations

$$\begin{aligned} \frac{d\epsilon_1}{dt} &= -(\alpha_1 + \alpha_2 + \beta_1)\epsilon_1 + (\beta_1 - \beta_2)\epsilon_2 + (\alpha_1 + \alpha_2)\epsilon_w \\ \frac{d\epsilon_2}{dt} &= -\alpha_2\epsilon_1 - \beta_2\epsilon_2 + \alpha_2\epsilon_w, \end{aligned} \tag{12}$$

where α_1, α_2, β_1 and β_2 are defined in Table 3. There are two timescales $\tau^a_{v_2}$ and $\tau^b_{v_2}$ associated with prediction of the nerve ending relaxation, thus one expects the BR firing rate to observe adaptation more closely. For this model represented by two Voigt bodies (E_j, η_j), $j = 1, 2$, in series with a spring E_0, those two time-scales can be computed as follows. The total strain-stress relationship is given by the following equation

$$a_2\epsilon''_w + a_1\epsilon'_w + a_0\epsilon_w = b_2\sigma'' + b_1\sigma' + b_0\sigma, \tag{13}$$

where the coefficients are

$$\begin{aligned} a_0 &= E_0E_1E_2 & b_0 &= E_0E_1 + E_0E_2 + E_1E_2 \\ a_1 &= E_0(E_1\eta_2 + E_2\eta_1) & b_1 &= E_0\eta 1 + E_0\eta_2 + E_1\eta_2 + E_2\eta_1 \\ a_2 &= E_0\,\eta_1\eta_2 & b_2 &= \eta_1\eta_2. \end{aligned}$$

For the step-increase in pressure (and thus wall stain ϵ_w) we obtain $\epsilon'_w = \epsilon''_w = 0$. Therefore the two timescales $\tau^a_{v_2}$ and $\tau^b_{v_2}$ are given by the roots of the characteristic equation

$$\xi_{V_2}(x) = [\alpha_2\beta_1 + \alpha_1\beta_2 + \beta_1\beta_2] + [\alpha_1 + \alpha_2 + \beta_1 + \beta_2]x + x^2. \tag{14}$$

Three Voigt body model (V_3). For model with three Voigt bodies in series with a spring (Figure 4 for $n = 3$) we obtain the following system of three differential equations

$$\begin{aligned} \frac{d\epsilon_1}{dt} &= -(\alpha_1 + \alpha_2 + \alpha_3 - \beta_1)\epsilon_1 + (\beta_1 - \beta_2)\epsilon_2 + (\beta_2 - \beta_3)\epsilon_3 + (\alpha_1 + \alpha_2 + \alpha_3)\epsilon_w \\ \frac{d\epsilon_2}{dt} &= -(\alpha_2 + \alpha_3)\epsilon_1 - \beta_2\epsilon_2 + (\beta_2 - \beta_3)\epsilon_3 + (\alpha_2 + \alpha_3)\epsilon_w \\ \frac{d\epsilon_3}{dt} &= -\alpha_3\epsilon_1 - \beta_3\epsilon_3 + \alpha_3\epsilon_w, \end{aligned} \tag{15}$$

where as in the previous case the coefficients $\alpha_j, \beta_j,\ j = 1, 2, 3$ are provided in Table 3. This model has three time-scales $\tau^a_{v_3}$, $\tau^b_{v_3}$ and $\tau^c_{v_3}$ associated with the nerve-ending relaxation. Again, the total strain-stress relationship for our model is given by

$$a_3\epsilon_w^{(3)} + a_2\epsilon_w'' + a_1\epsilon_w' + a_0\epsilon_w = b_3\sigma^{(3)} + b_2\sigma'' + b_1\sigma' + b_0\sigma, \tag{16}$$

where the coefficients are given by

$$\begin{aligned}
a_0 &= E_0E_1E_2E_3 & b_0 &= E_0E_1E_2 + E_0E_1E_3 + E_0E_2E_3 + E_1E_2E_3\\
a_1 &= E_0(E_2E_3\eta_1 + E_1E_3\eta_2 + E_1E_2\eta_3) & b_1 &= E_0E_2\eta_1 + E_0E_3\eta_1 + E_2E_3\eta_1 + E_0E_1\eta_2 + E_0E_3\eta_2 +\\
& & & \quad E_1E_3\eta_2 + E_0E_1\eta_3 + E_0E_2\eta_3 + E_1E_2\eta_3\\
a_2 &= E_0\left(E_3\eta_1\eta_2 + E_2\eta_1\eta_3 + E_1\eta_2\eta_3\right) & b_2 &= E_3\eta_1\eta_2 + E_0\eta_1\eta_2 + E_0\eta_1\eta_3 + E_2\eta_1\eta_3 + E_0\eta_2\eta_3 + E_1\eta_2\eta_3\\
a_3 &= E_0\,\eta_1\eta_2\eta_3 & b_3 &= \eta_1\eta_2\eta_3.
\end{aligned}$$

For the step-increase in pressure (and thus wall stain ϵ_w) w obtain $\epsilon_w' = \epsilon_w'' = \epsilon_w^{(3)} = 0$. Thus the timescales are the roots of the following characteristic equation

$$\xi_{V_3}(x) = A_0 + A_1x + A_2x^2 + x^3, \tag{17}$$

where

$$\begin{aligned}
A_0 &= \alpha_1\beta_2\beta_3 + \alpha_2\beta_1\beta_3 + \alpha_3\beta_1\beta_2 + \beta_1\beta_2\beta_3,\\
A_1 &= \alpha_1(\beta_2 + \beta_3) + \alpha_2(\beta_1 + \beta_3) + \alpha_3(\beta_1 + \beta_2) + \beta_1\beta_2 + \beta_1\beta_3 + \beta_2\beta_3,\\
A_2 &= \alpha_1 + \alpha_2 + \alpha_3 + \beta_1 + \beta_2 + \beta_3,
\end{aligned}$$

where again α_j, β_j $(j = 1, 3)$ are given in Table 3.

BR Firing rate

The final model component requires a description of the generation of action potentials in response to stimulation of the mechanoreceptors. The generation of action potentials is often described using the Hodgkin-Huxley (HH) model representing the biophysical characteristic of cell membranes, including a lipid bilayer represented by a capacitance and membrane channel proteins represented as nonlinear resistors. Action potentials are initiated when the neuron receives sufficient electrical current stimulus, in case of BRs, this stimulus is typically via pressure dependent stimulation of stretch sensitive ion channels. These detailed models are fairly complex and contain numerous parameters; moreover, they describe the dynamics of membrane voltage instead of directly modeling firing rate. In this study, we proceed proposing two models: a very simple model, that predicts firing rate linearly from the mechanoreceptor stimulation, and using a leaky integrate-and-fire model. The linear model simply amplifying the strain is denoted by N_a and the integrate-and-fire model denoted by N_{IF}.

Simple amplifier ($\mathbf{N_a}$). For the simplest possible model, we assume that action potential generation, and thus nerve firing rate, can be predicted by considering a simple linear amplifier described by

$$f = s_1\epsilon_{ne} - s_2, \tag{18}$$

where s_1 is the *gain*, and s_2 is the *shift*. The underlying assumption of this model is that the change in firing is proportional to the mechanical stimulation, ϵ_{ne}, of the nerve ending.

Leaky integrate-and-fire model ($\mathbf{N_{IF}}$). A more realistic description can be obtained using a leaky integrate-and-fire model, which considers the BR neuron as a simple electrically excitable membrane stimulated by a current generated by the mechanoreceptors. We assume that the generated current is proportional to the strain sensed by the nerve endings ϵ_{ne}. The leaky integrate-and-fire model originally

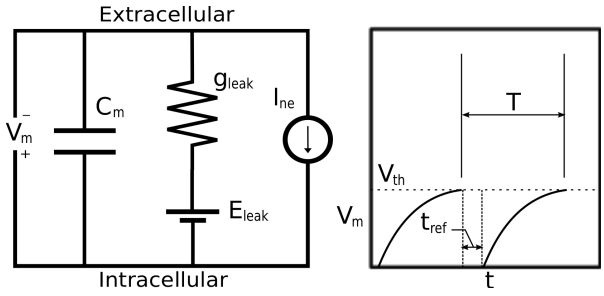

Figure 5. Diagram for leaky integrate-and-fire model. The circuit diagram (left) represents the schematic layout of the integrate-and-fire components. The graph (right) depicts voltage vs time for a neuron stimulated by a constant current.

proposed by Lapicque [63], but also discussed by [64, 65], describes the excitation of the voltage across the BR membrane. The membrane voltage is equivalent to the voltage across a capacitor in an RC circuit (Figure 5) with a stimulus current (given as a function of ϵ_{ne}) and an Ohmic leakage current, generated by the difference of the membrane potential and the rest potential, 0 mV.

The change in voltage generated by a leaky integrate-and-fire model is predicted as

$$C_m \frac{dV_m}{dt} = I_{ne} - g_{leak} V_m, \tag{19}$$

where I_{ne} denotes the current stimulus, g_{leak} is a leakage conductance, and C_m denotes the membrane capacitance. In the equation above, the voltage V_m is relative to the equilibrium potential. To model the firing rate of the neuron we assume that to form an action potential, the BR neuron has to charge the membrane voltage above a given voltage threshold, which we denote V_{th}. Applying this assumption to (19), allows prediction of T, i.e., time required for the voltage to increase from equilibrium to the threshold, for a given stimulus current, I_{ne}. We can find T integrating (19), i.e.,

$$\int_0^{V_{th}} \frac{dV_m}{I_{ne} - g_{leak} V_m} = \int_0^{T} \frac{dt}{C_m}. \tag{20}$$

For constant I_{ne} this equation can be solved analytically, yielding

$$T = \frac{C_m}{g_{leak}} \Big[\ln\left(I_{ne} - g_{leak} V_{th}\right) - \ln\left(I_{ne}\right) \Big],$$

where, as stated above, T represents the time required to generate an action potential given a constant current stimulus I_{ne}. We propose to model I_{ne} as a linear function of ϵ_{ne}

$$I_{ne} = \bar{s}_1 \epsilon_{ne} + \bar{s}_2. \tag{21}$$

Finally, the absolute refractory period t_{ref}, i.e., the time following an action potential, during which a subsequent action potential cannot be generated [66] should be accounted for. This can be done by letting the rate (frequency) $f = (T + t_{ref})^{-1}$. With these simplifying assumptions the BR firing rate can be predicted as a function of the instantaneous strain of the nerve ending sensed by the BR as

$$f = \begin{cases} \left[\frac{C_m}{g_{leak}} \left[\ln\left(\frac{I_{ne} - g_{leak} V_{th}}{I_{ne}} \right) \right] + t_{ref} \right]^{-1} & I_{ne} > g_{leak} V_{th} \\ 0 & \text{otherwise.} \end{cases} \tag{22}$$

We propose to interpret the BR firing rate as that given by (22) for I_{ne} at a given instant. The piecewise definition of the frequency is necessary as (20) does not have a solution when the stimulus current is less than the leak current at threshold voltage. This is a consistent interpretation of the instantaneous frequency as we do not expect any firing events to occur for a sub-threshold stimulus (less than the base current). In general, for a sub-threshold current stimulus the firing f is expected to cease until I_{ne} is increased above the threshold level. The parameters C_m, g_{leak}, t_{ref}, and V_{th} of this model are expected to approximately correspond to the electrophysiologically observable characteristics of the BR neuron, membrane capacitance, leakage conductance, refractory period and threshold, respectively. The membrane capacitance can be measured using electrophysiological techniques [67]. Leakage conductance can be approximated as the net inward conductance near equilibrium potential. The true refractory period and threshold voltage of a neuron are not absolute and are typically somewhat dynamic and thus difficult to measure. One may roughly estimate these values for BRs from the results of experimental studies of the membrane excitability of nodose neurons, a neuron family including BRs [67]. The observation of BR firing rates up to 140 Hz leads to a refectory period of $t_{ref} \approx 7$ msec [21, 22].

Composite BR models

In the previous sections we developed a framework to model the three main components involved with prediction of BR firing. To develop a composite model, one component must be chosen from each category. There are various options one may select from in order to construct a BR model. The choice depends on a number of factors including the type of species (e.g., rats, dogs, sheep, humans, etc.) and the type of data (e.g., steady, step-change, dynamic, in-vivo, etc.). We propose a total of six linear and nonlinear models, summarized in Table 2, which we will carefully analyze and test using aortic baroreceptor rat data. These models can be formulated as a system of algebraic and differential equations of the form

$$\begin{aligned} \epsilon_w &= g_1(p, t; \theta) \\ \frac{dx}{dt} &= g_2(x, \epsilon_w, t; \theta) \\ f(x, t; \theta) &= g_3(x, t; \theta), \end{aligned} \tag{23}$$

where p the blood pressure (model input); ϵ_w denotes the vessel strain; $x = (\epsilon_1, \epsilon_2, ..., \epsilon_n)$; t time (sec); θ the model parameters; and f the BR firing rate. Models can be separated in two basic types: linear and nonlinear models. It should be noted that differential equations only enter via the model component describing mechanoreceptor strain. To ensure that model simulation began from a relaxed state, we computed the initial conditions by solving $g_2(x, g_1(p, t; \theta), t; \theta) = 0$. To be more precise for the four linear BR models $W_eV_1N_a$, $W_eV_2N_a$, $W_eV_3N_a$, and $W_{ve}V_3N_a$ initial conditions are respectively

$$\begin{aligned} x^*_{V1} &= -\alpha_1 k_w p_M/(\alpha_1 + \beta_1) \\ x^*_{V2} &= \frac{k_w p_M}{\alpha_2\beta_1 + (\alpha_1 + \beta_1)\beta_2}\Big[\alpha_2\beta_1 + \alpha_1\beta_2, \quad \alpha_2\beta_1\Big]^\top \\ x^*_{V3} &= \frac{k_w p_M}{\alpha_3\beta_1\beta_2 + (\alpha_2\beta_1 + (\alpha_1 + \beta_1)\beta_2)\beta_3}\Big[\alpha_3\beta_1\beta_2 + \alpha_2\beta_1\beta_3 + \alpha_1\beta_2\beta_3, \quad \beta_1(\alpha_3\beta_2 + \alpha_2\beta_3), \quad \alpha_3\beta_1\beta_2\Big]^\top \\ x^*_{ve} &= \frac{k_w(p_M + \tau_b\, p_D)}{\alpha_2\beta_1 + (\alpha_1 + \beta_1)\beta_2}\Big[\alpha_2\beta_1 + \alpha_1\beta_2, \quad \alpha_2\beta_1\Big]^\top \end{aligned}$$

where p_M and p_D are the initial values of the pressure stimulus and its derivative, respectively, and τ_b, α_j, β_j, for $j = 1, 2, 3$ are given in Table 3. For the nonlinear model $W_{ne}V_2N_a$ we used the following initial condition

$$x^*_{ne} = \frac{I_n}{\alpha_2\beta_1 + (\alpha_1 + \beta_1)\beta_2}\Big[\alpha_2\beta_1 + \alpha_1\beta_2, \quad \alpha_2\beta_1\Big]^\top, \qquad I_n = 1 - \Big[A_0(\alpha^\kappa + p_M^\kappa)/(A_0\alpha^\kappa + A_m p_M^\kappa)\Big].$$

Table 2. Summary of the BR models.

Model	Wall	Nerve ending	Neuron	Parameters
$W_eV_1N_a$	Eq (4)	Eq (10) & (9)	Eq (18)	$k_{wall}, \alpha_1, \beta_1, s_1, s_2$
$W_eV_2N_a$	Eq (4)	Eq (12) & (9)	Eq (18)	$k_{wall}, \alpha_1, \alpha_2, \beta_1, \beta_2, s_1, s_2$
$W_eV_3N_a$	Eq (4)	Eq (15) & (9)	Eq (18)	$k_{wall}, \alpha_1, \alpha_2, \alpha_3, \beta_1, \beta_2, \beta_3, s_1, s_2$
$W_{ve}V_2N_a$	Eq (7)	Eq (15) & (9)	Eq (18)	$k_{wall}, \tau_a, \tau_b, \alpha_1, \alpha_2, \beta_1, \beta_2, s_1, s_2$
$W_{ne}V_2N_a$	Eq (5)	Eq (15) & (9)	Eq (18)	$A_0, A_m, \alpha, k, \alpha_1, \alpha_2, \beta_1, \beta_2, s_1, s_2$
$W_{ne}V_2N_{IF}$	Eq (5)	Eq (15) & (9)	Eq (22)	$A_0, A_m, \alpha, k, \alpha_1, \alpha_2, \beta_1, \beta_2, \bar{s}_1, \bar{s}_2, C_m, g_{rec}, V_{th}, t_{ref}$

The table defines six BR models that are tested against previously recorded BR data from rats [30]. Each model is denoted by a three-element name referring to a corresponding part of its component (arterial wall W, mechanoreceptor stimulation V, neuron N). The cross-reference indicates what equation is included in a given model.

Results

In this section we present results obtained with the models introduced in the Method section and summarized in Table 2. First, we test the models' abilities to quantitatively predict experimental data with sinusoidal and step-increase stimuli. Second, we discuss the models's ability to predict qualitative features not encompassed by the quantitative data. Quantitative simulations allows us to highlight the components necessary predict observed data, whereas qualitative simulations allows us to test the model further in response to stimuli not detailed by experimental measurements.

Quantitative predictions

Models will be tested quantitatively using three types of pressure stimulus: sinusoidal at a fixed frequency, a step-increase, and a step-increase followed by a step decrease (Figure 2a-c). We investigated six linear and nonlinear models summarized in Table 2. For the wall strain three models were investigated, the simplest assumes the wall strain ϵ_w has a spring-like response (denoted W_e). The second model (denoted W_{ne}) accounts sigmoidally for increased stiffening with increased pressure, and finally we investigate a viscoelastic model (W_{ve}). The mechanoreceptor strain ϵ_{ne}, is modeled using one, two, and three Voigt bodies, respectively, in series with the spring (V_1, V_2, V_3). Finally, two models were used for prediction of BR firing rate, a linear model (N_a) and an integrate-and-fire model (N_{IF}). As mentioned above, these models can all be described as a system of algebraic and differential equations. For all models the model input is pressure p and the model output is BR firing rate f, initial conditions were computed to ensure that model solutions start at steady state. For quantitative predictions, the objective was to estimate model parameters minimizing the least squares error between the model and data. Since data is only available for the BR firing rate and the pressure stimuli, for most models not all parameters are identifiable. We denote as identifiable parameters, those that are sensitive and not correlated, given the model output and the associated available data [68]. In this study, identifiability of parameters was determined using sensitivity based methods [69]. Subsequently, for models completely characterized by smooth functions, the Levenberg-Marquart method was used to estimate model parameters, while for models not fulfilling this requirement (the integrate-and-fire models), parameters were estimated using the Nelder-Mead method. Both used optimization algorithms from Kelley [70].

Below we first describe the methodology used for sensitivity analysis and parameter identification and subsequently we discuss results obtained using nonlinear optimization, the latter is separated according to the input stimulus.

Sensitivity analysis: For any smooth model of the form (23), the sensitivities [71–73] can be computed as

$$S_k = \frac{\partial f}{\partial \theta_k}.$$

Following Pope et al. [74], we use a finite difference approximation to compute S_k

$$S_k = \frac{f(t, \theta + he_k) - f(t, \theta)}{h}, \qquad e_k = \left[0 \dots 0 \overset{k}{\widehat{1}} 0 \dots 0\right]^T,$$

where e_k is the unit vector in the k^{th} component direction and h is a small number. The BR firing rate f is obtained computationally, with an integration tolerance of $\chi = 10^{-6}$ imposed on solution of the differential equations, thus h is bounded by $\sqrt{\chi}$. To satisfy this requirement we let $h = 0.01$.

Sensitivities are ranked by averaging time-varying functions using the two-norm. For each model, this ranking was used to separate parameters into two groups: one group consisted of parameters to which the model output was sensitive, and the other group consisted of parameters to which the model output was insensitive. Estimating only sensitive parameters gives rise to more reliable parameter estimates [75].

Not all sensitive parameters are practically identifiable [68,69]. To identify parameter correlations, we used subset selection method [74,76,77]. We also used a method based on covariance analysis to identify pairs of correlated parameters [69]. For each pair of correlated parameters the least sensitive parameter was kept fixed at its nominal value while the other was included in the subset. Parameter correlations were predicted from

$$c_{i,j} = \frac{C_{i,j}}{\sqrt{C_{i,i}C_{j,j}}}, \qquad C = \sigma(S^T S)^{-1},$$

where σ is the variance of the assumed noise in the data, C is the covariance matrix, and is $c_{i,j}$ the correlation coefficient. Parameters for which $|c_{i,j}| > \gamma$ are labeled as correlated. For the models studied in this work we let $\gamma = 0.8$. Once a set of uncorrelated sensitive parameters were identified, we used either the Levenberg-Marquart or the Nelder-Mead method to estimate the subset of practically identifiable model parameters [70]. The Levenberg-Marquart method was used for models that can be described using smooth functions, while the Nelder-Mead method was used for models including the leaky integrate-and-fire component. Since this model contains a discontinuity in prediction of the firing rate f, thus the gradient based Levenberg-Marquart method is not applicable.

Sinusoidal stimulus: Now we present results obtained using sinusoidal forcing allowing us investigate asymmetry of the model response. Results (Figure 6) show BR firing rate as a function of time and BR firing rate as a function of stimulus. For both graphs model results are marked with red lines and data with black. The associated pressure stimulus is depicted in Figure 2a. For this stimulus we analyzed five models. We first describe results obtained with the three linear models, analyzing the impact of including one, two, or three Voigt bodies, second we discuss results obtained with the nonlinear models analyzing the impact of including more advanced models predicting the wall strain. For this stimulus we did not analyze the integrate-and-fire model, since we did not anticipate any added effect of this model because of the input rage of the pressure stimulus.

The three linear models predicts wall strain using a linear elastic function of pressure, combined with one, two, and three Voigt bodies, for prediction of mechanoreceptor stimulation, and a linear model for prediction of the BR firing rate. The three models have 5, 7, and 9 parameters, respectively, as well as two additional parameters p_1 and p_2 associated with the sinusoidal stimulus. In [20, p. 695] the authors indicated that phase measurements are less accurate than amplitude measurements due to the inaccuracies associated with assigning interspike intervals to bins. This statement made us add the parameters p_1 and p_2 to the parameter set. Sensitivity analysis together with subset selection method identified four uncorrelated parameters including s_1, s_2, p_1, and p_2, which were estimated for all three models.

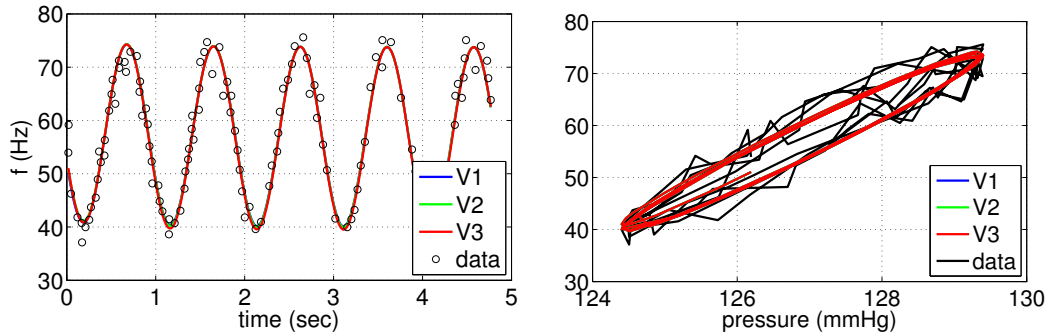

Figure 6. The optimized response of linear BR models, and the corresponding hysteresis loop. We present the fits for three linear BR models $W_eV_1N_a$, $W_eV_2N_a$ and $W_eV_3N_a$ (denoted in the legend as V1, V2, and V3, respectively), listed in Table 2. The optimized parameter values, the R^2 and the RMSE errors are reported in Table 4.

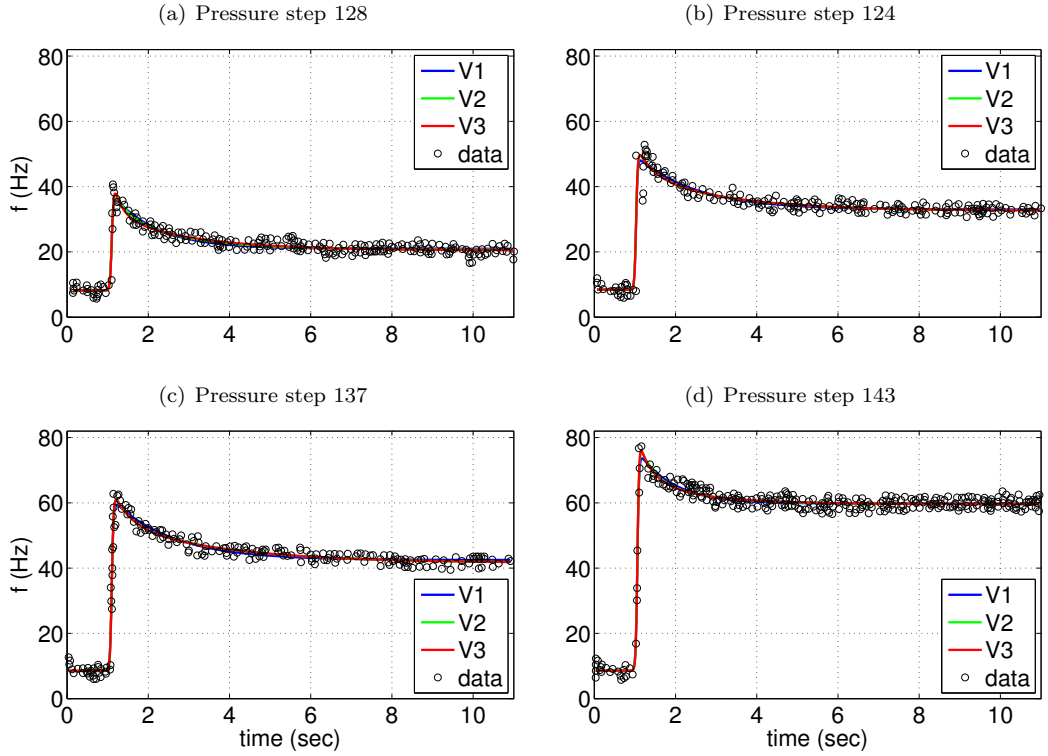

Figure 7. The optimized response of linear BR models. We show the ability of three linear models $W_eV_1N_a$, $W_eV_2N_a$ and $W_eV_3N_a$ (denoted in the legend as V1, V2, and V3, respectively) to reproduce four types of increases in pressure published by Brown [20] (denoted as BR). The parameters of each model have been optimized for each data set individually and are listed in Table 4 together with the R^2 and the RMSE errors.

The nominal values for the model parameters (listed in Table 4) were computed as follows. The parameter $k_{wall} = r_0/Eh$, where E is Young's modulus, h is a wall thickness, and r_0 is a zero pressure radius (described in the Methods section). In [78, Table 1] Bezie et al. compute Young's modulus in the aorta obtaining $E = 820 \pm 70$ for 11 spontaneously hypertensive rats (SHR); and $E = 1280 \pm 140$ for 19 normotensive Wistar rats; here the mean is given $\pm$ standard error of the mean (REM). As expected, for the two strains the difference in E was significant; SHR had a higher modulus, representing stiffer vessels, than the normotensive rats. Using this data we computed the average value $E = 1050$, obtained at mean pressure stimulus of 132 mmHg, and standard deviation (SD) of 19.2, which was computed by converting REM to SD ($SD = REM/\sqrt{n}$, n is a population size) and then taking the average of the two populations, assuming they are normally distributed. In [79, Figure 1] Feng et al. provide detailed measurements of the external diameter D and thickness h for the rat aortic arch, measured in adult male Sprague-Dawley rats. They found that in the region with aortic BR endings the average values of $D = 2.27 \pm 0.17$ and $h = 0.17 \pm 0.02$. Using these values we compute $k_{wall} = 0.0063$. No direct experiments exist allowing estimation of nominal values for the elastic E_1, E_2, E_3 and viscous constants η_1, η_2, η_3 associated with prediction of mechanoreceptor strain. These parameters appear only in the dynamic part of the model and determine the adaptation time-scales. To ensure that the three models are distinct, it is essential that parameters representing time-scales are separated, otherwise the models would essentially reduce to one. This knowledge, along with values chosen in the study by Bugenhagen et al. [59] motivated our choice for nominal parameter values. To avoid the problem of structural nonidentifiability [68] we rescaled the parameters as follows $\alpha_j = E_0/\eta_j$ and $\beta_j = E_j/\eta_j$ for $j = 1, 2, 3$. The full list of the model parameters together with their initial conditions, units and literature reference is provided in Table 3. As for the stimulus, the average pressure (127 mmHg) and the amplitude (5 mmHg) was provided in [20]. To compute the frequency p_1 and the shift p_2 of the pressure, we digitized the stimulus provided in [20, Figure 2A], and then fitted to a sinusoidal function $p(t) = -2.5\sin(-p_1 t + p_2) + 127$, obtaining $p_1 = 6.45$ and $p_2 = 46.75$. As noted in Figure 6, results of parameter estimation with each of the three models were indistinguishable, though estimated parameter values varied significantly, the latter is due to added complexity associated with adding more Voigt bodies. The fact that graphs were almost identical was also reflected by the least squares cost RMSE (and the coefficient of determination R^2) for models $W_e V_1 N_a$, $W_e V_2 N_a$ and $W_e V_3 N_a$ we obtained 2.522 (0.949), 2.507 (0.950), and 2.495 (0.951), respectively, see Table 4.

Next, we investigated the impact of including a more complex wall mode. Two additional models were analyzed predicting wall strain as a nonlinear function of pressure and accounting for viscous damping allowing wall deformation to be nonlinear W_{ne} and viscoelastic W_{ve}. Keeping the number of Voigt bodies and the BR firing rate model constant resulted in a comparison with three models including $W_e V_2 N_a$, $W_{ve} V_2 N_a$ and $W_{ne} V_2 N_a$ described using 7, 8, 9 parameters plus the two parameters associated with the stimulus. We examined the ability of each of these models to fit the sinusoidal stimulus. Sensitivity analysis and subset selection allowed us to estimate 4-6 parameters. All models allowed us to estimate s_1, s_2, p_1, and p_2. In addition, for the nonlinear elastic model A_m was added to the subset and for the viscoelastic model τ_a and τ_b was added to the subset. Given that the more complex nonlinear models allows estimation of more parameters, one should anticipate better results. But due to the limited dynamics embedded within the pressure stimulus, adding more complex wall models did not improve results as reflected by the least squares cost RMSE (and the coefficient of determination R^2), which for $W_e V_2 N_a$, $W_{ve} V_2 N_a$ and $W_{ne} V_2 N_a$ gave 2.507 (0.950), 2.517 (0.950), and 2.458 (0.952), respectively; see Table 5.

Step-increase stimulus: This section presents results with the same five models used for predictions with the sinusoidal pressure stimulus. As with the sinusoidal stimulus we do not test the integrate-and-fire model, due to the nature of the input stimulus. Again, we first discuss results obtained with the three linear models $W_e V_1 N_a$, $W_e V_2 N_a$ and $W_e V_3 N_a$ followed by results obtained using the more complex nonlinear and viscoelastic wall models.

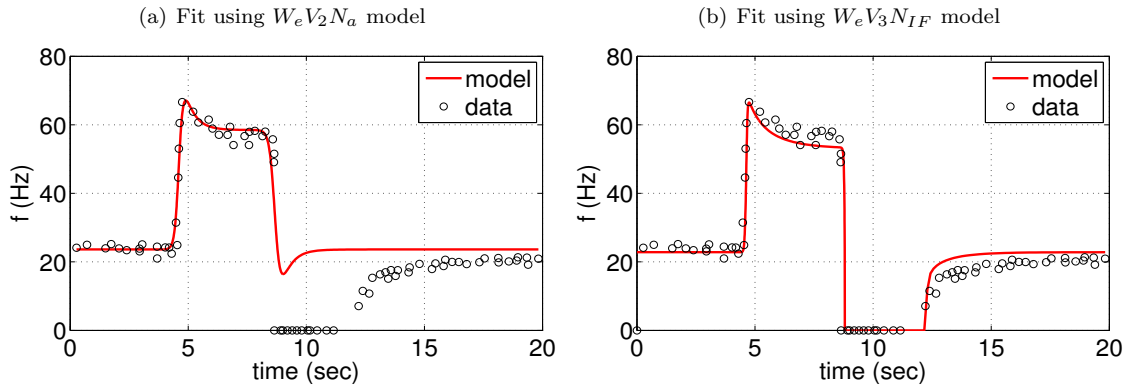

Figure 8. The optimized response of (a) $W_eV_2N_a$, and (b) and $W_eV_3N_{IF}$ to a PED profile of BR firing rate. The parameters of each model have been optimized for each data set individually and are given in Table 4 together with the R^2 and the RMSE errors.

Studies were done to capture the effect of overshoot and adaptation in response to four input stimuli varying in the magnitude of the pressure step. All stimuli start at the same baseline pressure, and the step-increase was imposed at the same time t_0. As before the three models have 5, 7, and 9 parameters, respectively, but functions predicting the "smooth" step pressure increase only involve one additional parameter δ_u, representing the onset of the step-increase. This parameter was not provided in [20]. Subset selection together with efforts to make model comparison possible resulted in $\theta_{step} = \{\alpha_1, \beta_1, s_1, s_2, \delta_u\}$. As reported in [20, Figure 5] the baseline pressure associated with the step-increase stimulus was set to 115 mmHg, and the step-increases (from the baseline) to 128, 134, 137, 143 mmHg, respectively. Figure 7(a-d) shows the ability of the three linear BR models to reflect observed overshoot and adaptation. Each panel shows the optimized firing rate. The least squares cost RMSE (and the coefficient of determination R^2) of model $W_eV_1N_a$ for the optimized values of its parameters with respect to the four step-increases 128, 134, 137, and 143 mmHg were: 1.860 (0.899), 2.677 (0.919), 2.420 (0.969), and 1.832 (0.983). Marginal improvements were obtained with $W_eV_2N_a$, which gave: 1.800 (0.905), 2.702 (0.917), 2.390 (0.970), and 1.823 (0.983), and finally, for $W_eV_3N_a$ the values were: 1.764 (0.909), 2.700 (0.918), 2.390 (0.970), and 1.809 (0.983), see Table 4. Similar to the sigmoidal stimulus, no improvements (results not shown) were obtained with the more advanced nonlinear and viscoelsatic wall models.

Square stimulus: The square stimulus is characterized by a constant pressure input followed by a step-increase after which the pressure is decreased to its baseline value. This type of stimulus primarily tested the models' ability to reflect PED followed by recovery, although other features including adaptation and overshoot are also shown. Similar to previous studies we first investigated the simpler linear models including one, two and three Voigt bodies. For the square input stimulus, in Figure 8a, we plot BR firing rate data extracted from Saum et al. [32] (circles) and the corresponding optimized fit using $W_eV_2N_a$ (solid line), changing the number of Voigt bodies did not improve model predictions. This model has 7 parameters and additional two δ_u and δ_d related with the input stimulus (3). Subset selection together with our effort to make model comparisons possible made us estimate the parameters $\theta_{square} = \{s_1, s_2, \delta_u, \delta_d\}$. The least squares cost RMSE (and the coefficient R^2) with optimized parameters was 7.384 (0.862 for R^2), see Table 6. While the model, as anticipated, was able to predict overshoot and adaptation, this model was not able to capture PED accurately.

We hypothesize that the inability to predict PED is due to the simple linear firing rate model, which does not allow the BR firing rate to cease for sub-threshold stimuli. Thus, we first investigated the impact of exchanging the linear BR firing rate model with the integrate-and-fire model. Including the integrate-and-fire model clearly improved results (not shown) though with the linear wall model it was

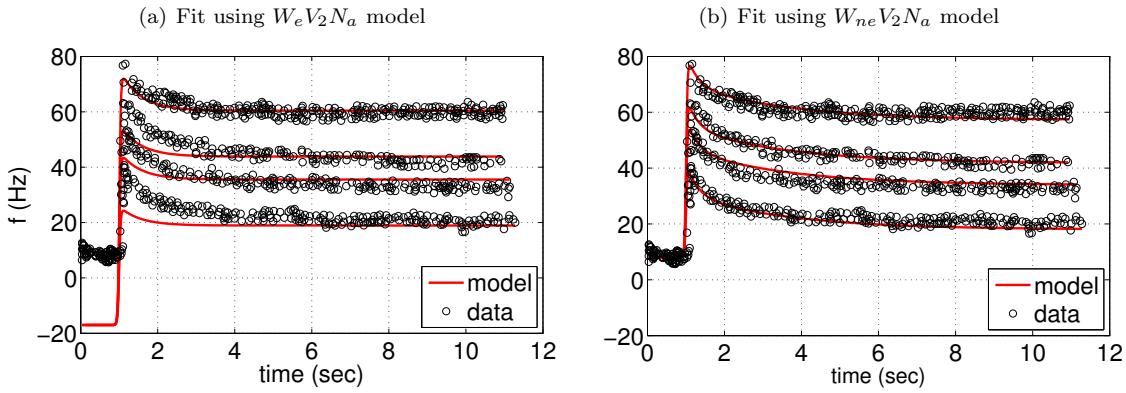

Figure 9. Simultaneous response with a linear and a nonlinear BR model. (a) Predictions obtained estimating one parameter set for all four pressure step-increases using the linear model with two Voigt bodies $W_eV_2N_a$. Note, that the overshoot is diminished for responses to smaller step-increases in pressure, and that the baseline firing rate is not predicted accurately. (b) Predictions obtained with the nonlinear model $W_{ne}V_2N_a$ accounting for nonlinear stiffening with increased pressure allowed us to accurately predict all four responses using one set of parameter values.

difficult to accurately predict response both during adaptation and recovery. Subsequently, we analyzed the impact of exchanging the linear wall model with the nonlinear wall model, keeping the integrate-and-fire model. Results with this model ($W_{ne}V_2N_{IF}$) is shown in Figure 8b. This figure shows the recorded BR firing rate (circles) and the model fit (solid line) in response to the square pulse stimulus. Model parameters estimated include $A_0, \bar{s}_1, \bar{s}_2, g_{leak}, V_{th}, t_{ref}, p_u, p_d$. Optimized parameter values are given in Table 6 together with the R^2 and RMSE errors. Finally, we investigated the impact of adding a viscoelastic wall model, which did not provide any additional improvements.

Simultaneous fits: Figure 7 showed that linear models can exhibit overshoot, adaptation, and can predict the firing rate data for all four step-increases, though as reported in Table 4, each step-increase resulted in significantly different parameter estimates. However, data are extracted from experiments done within the same fiber, thus we expected only small variation in parameter values. We performed additional optimizations to investigate if the observed differences in the parameter estimates, were simply a result of performing optimizations for one stimulus at the time. To remedy this problem, we estimated one set of parameters for all four step-increases. Results of this simulation are shown in Figure 9a (computed with the model $W_eV_2N_a$). This simulation confirms that the simple linear model cannot estimate one set of parameters that allows *simultaneous* prediction of the response to all four pressure stimuli. Similar results were obtained with the other models. In particular, it should be noted that the overshoot is diminished for the smaller step-increases, and that the model was unable to capture the correct baseline firing rate. In contrast, when including a nonlinear elastic wall $W_{ne}V_2N_a$ we were able to estimate one set of parameters that allowed us to simultaneous fit the response to all four pressure stimuli. This model accurately reproduced the baseline firing rate as well as the overshoot and adaptation observed in response to the step-increase (Figure 9b). We hypothesize that this difference is due to larger range of pressure within the applied stimuli, where the known nonlinear behavior of the arterial wall deformation plays an important role. It is known that arteries appear stiffer at higher pressures than at lower pressure. Thus the nonlinear wall model significantly improves predictions.

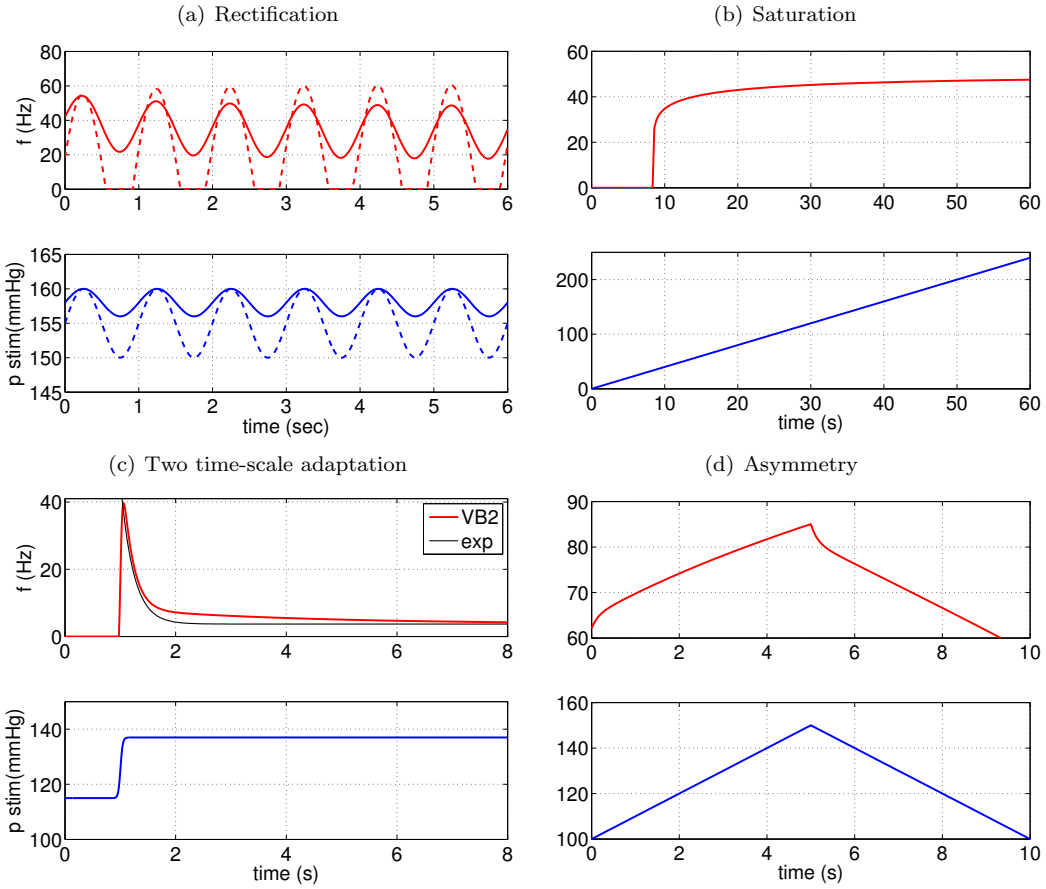

Figure 10. Qualitative responses. We present a qualitative response of the two Voigt body BR model $W_{ne}V_2N_{IF}$ to various pressure stimuli including sinusoidal (a), ramp up (b), step-increase (c), and trianglular (d) showing the models ability to reflect rectification (a), saturation (b), two time-scale adaptation (c), and asymmetry (d).

Qualitative predictions

In the previous section we showed the ability of our proposed linear and nonlinear BR models to predict the firing rate data measured from rats. It is well known (see section Methods) that the BR firing rate can exhibit a number of qualitative characteristics including saturation, threshold, adaptation, overshoot, PED and rectification. The quantitative data used to test the model in the previous section showed adaptation, overshoot, and PED, in response to a sinusoidal (with fixed amplitude) and step changes (increase/decrease) in blood pressure. However, these stimuli did not test saturation, threshold, or rectification. Although the models predicted adaptation, no clear conclusion could be drawn to determine how many Voigt elements (time-scales) were needed to predict known BR firing rate observations.

In this section we show our preferred model $W_{ne}V_2N_{IF}$ with estimated parameters, including nonlinear deformation of the elastic wall, two Voigt bodies for predicting nerve ending stimulation, and a leaky integrate-and-fire model for predicting firing rate, exhibits the features not already predicted quantitatively. This was done using ramp and sinusoidal (with varied amplitude and frequency) pressure stimuli.

Rectification: Figure 10a presents the model's response to a sinusoidal wave pressure stimulus with various amplitude. This simulation is motivated by the observation of Brown et al. [20, Figure 6] that a 2.5 increase in amplitude of the sinusoidal stimulus resulted in an increased amplitude of the firing rate, with a lower mean firing rate. Moreover, it was noted that for large amplitude stimulation the firing rate ceases during the trough of the pressure wave. These two observations are referred to as rectification. One could question if the simpler linear model is able to predict this phenomena. The linear wall model would certainly be able to reproduce the increased amplitude for a single stimulus, but again, if multiple stimuli were tested, correct prediction requires the nonlinear wall model. Moreover, the ability of the firing rate to cease requires the threshold built into the integrate-and-fire model. With the simple linear neuron model, the firing rate would become negative, which does not represent what happens physiologically.

Threshold and saturation: Two other prominent firing characteristics are threshold and saturation. In [27, Figure 5] Seagard et al. noted that BRs with a higher threshold pressure were less sensitive, had lower discharge rates, and had higher values for saturation. Receptors with higher discharge rates were also more sensitive and were found to have afferent fibers with greater conduction velocities, shown to the right of each curve. In Figure 10b we show that our model $W_{ne}V_2N_{IF}$ is able to reproduce qualitatively similar saturation features.

Adaptation: Even though our quantitative models were able to predict adaptation, it was noted that results with one, two, or three Voigt bodies were similar, in other words, the models could not clearly distinguish if the adaptation process included one or three time-scales. Yet, several authors (e.g., [11, 12, 29, 80]) have hypothesized that adaptation occurs with more then one time constant. It is also known that the muscle spindle can produce a response of this kind to a clipped-off ramp stretch [81]. Figure 10(c) shows that the studied model $W_{ne}V_2N_{IF}$ admits the fast adaptation and the slow adaptation in agreement with experiments. We also plot an exponential fit and show that a similar adaptation is not possible by only one exponential function. This qualitative feature made us include two Voigt bodies in our preferred model, a conclusion that could not have been made strictly from quantitative simulations presented in the previous section.

Asymmetry: In Figure 10(d) we show that our preferred model $W_{ne}V_2N_{IF}$ clearly predicts asymmetry when exposed to a ramp-up followed by a ramp-down pressure stimulus, which agrees with experiments (see e.g., [23]).

Discussion

The objective of this study was to develop a *mathematical framework* for constructing computationally efficient and accurate BR models, which in contrast to the existent models, are able to reflect *all* known qualitative BR firing features as well as fit quantitative data. Our overall aim was not to focus on a concrete experimental species but rather to formulate a family of BR models, which could potentially be included in a more comprehensive model of CV system. Quantitative predictions were done comparing our models to experimental measurements by Brown et al. [20] and Saum et al. [32]; while qualitative predictions were performed to show that our preferred generic model $W_{ne}V_2N_{IF}$ is able to predict all known firing rate responses. All models used blood pressure as an input and computed the BR firing rate as an output. Although our procedure was designed to be generically applicable to various species and multiple types of baroreceptors, we tested our models using only quantitative data from experiments preformed using aortic baroreceptors from rats.

We believe that this is the first work that offers a systematic approach to building and evaluating BR models with the objective to provide the simplest possible family of generic models. Our modeling framework first analyzed the known physiology and common features of the firing rate observed in the BR of various species. Second we generated sub-models predicting each stage of the physiological response: arterial wall deformation, stimulation of mechanosensitive channels found in the BR nerve endings, and generation of action potentials. Finally we modeled the BR system by combining the sub-models in

various configurations (summarized in Table 2). Each of these configurations was tested in order to see what were the contributions of each component to the transduction of the BR signal. This process allowed identification of the importance of nonlinear effects of two critical sub-systems in the BR response, the arterial wall and the neuron itself. This framework advanced the state of BR modeling by first evaluating models comparatively with respect to the same data and features, second by generating a model which fits all known characteristics of BR firing qualitatively, and third by developing a model which is capable of fitting multiple data sets of BR firing rates quantitatively.

A particular insight was revealed by consideration of BR models with various descriptions of the arterial wall. Applying our framework demonstrated the insufficiency of linear wall models' representations of the response of a single BR neuron to multiple step-pressure inputs (see Figure 9a). A nonlinear elastic wall model was required to implement a model capable of accurately fitting the BR response to multiple pressure levels with one set of parameter values (see Figure 9b). The choice of this model is further motivated by the well known fact that arteries exhibit nonlinear deformation with saturation at both high and low pressures [23, 27]. Additionally by applying our framework and considering the effects of including the viscoelastic wall model, we found that the additional complexity did not contribute to better definition of BR dynamics, despite previous studies having shown wall deformation does have viscous components [49, 82]. This is likely due to our modeling choice for nerve ending stimulation. This portion was modeled using two Voigt bodies in series to allow prediction of adaptation at multiple time-scales. Data is not available to separate the viscoelastic part of the wall-deformation with the viscoelastic deformation associated with stimulation of the mechanosensitive channels, thus indirectly our model exhibits both features. One explanation would consider the first Voigt body to be associated with wall deformation while the second is associated with nerve ending deformation. Moreover, it should be emphasized qualitative simulations were needed to show that the two Voigt bodies allow multiple time-scales, a feature that we were not able to extract from simulations alone. These considerations, and our studies, affirm the importance of viscoelastic effects; however, in terms of simplicity it is advantageous to isolate the viscoelastic components within the model, and further we note linear viscoelastic effects are sufficient to capture the dynamics of BR firing when coupled with a nonlinear elastic total deformation of the arterial wall.

To our knowledge, this study provides the first direct measure of the importance of incorporating various time-scales in BR models. It is believed that various time-scales in the adaptation process are due to the viscoelastic coupling of the nerve ending to the arterial wall. We chose to emphasize this in our modeling process by considering different numbers of Voigt bodies in series with a spring. In Table 4 we show the results of testing three models $W_eV_1N_a$, $W_eV_2N_a$, and $W_eV_3N_a$ differing only with respect to their nerve ending models V_1, V_2, and V_3, respectively. Our findings indicate that no more then two timescales in the adaptation process are needed in order to achieve a very precise fit to the data. This conclusion is closely related to the fact that we tested our models using rat data with fairly limited pressure-stimulus response as only this type of experiments are currently available. To test this component more carefully, it is essential to analyze data recorded over longer time- scales.

Another insight afforded by this investigation highlights the importance of nonlinearities in the neural response to mechanoreceptor strain. As hypothesized previously [29], our study affirms the nonlinearities of action potential generation, even for the leaky integrate-and-fire model N_{IF} are sufficient to produce the hysteretic phenomena of PED. In contrast the simple linear model N_a of firing in response to mechanoreceptor strain does not allow for the asymmetric responses seen in PED as well as in the response to sinusoidal stimulus with high amplitude. The nonlinear-elastic wall in combination with two Voigt bodies modeling mechanoreceptor stimulation responds in an equal but opposite manner to rising and falling pressure, thus the change in firing rate with the linear model is symmetric to step-increase and step-decrease, which is not reflective of the data. We affirm the hypothesis that the neuron itself is responsible for generating PED, as this feature was robustly represented by the leaky integrate-and-fire model regardless of the mathematical description for arterial wall strain. This would provide a good ex-

planation for the observation of PED in multiple species, many of which have a high degree of variability in the viscoelasticity in their respective arterial walls.

The results and insights generated through application of our proposed modeling framework are not limited to those presented in this study. In addition it provides a means to identify which features and what level of detail of the underlying physiological systems are of greatest significance in generating BR dynamics. This ability is useful in developing experiments which may be able to isolate physiology responsible for a given phenomenon, such as the responsibility of the neuron in generating PED. Further this approach provides evaluative power to make design decisions when developing a model for a specific data interpretation or simulation task. An example of this follows from our insights into the role of the arterial wall in BR signal transduction. Although the arterial wall may best be modeled using viscoelastic theory, our framework allows a modeling decision to be made in favor of simplicity if only the output dynamics are of interested.

Our results further suggest a methodology for integrating a model generated in this manner into a model of larger scope. Suppose a mathematical representation of an overall baroreflex system (see Figure 1) is desired to reflect only normal physiological conditions, then it may be sufficient to use only simplified description of the BR signal. For example a simple linear firing rate model may be adequate for simulations, which do not cross the firing rate threshold. However, to reflect heart rate at various abnormal physiological conditions a more complex model combining nonlinear deformation with the leaky integrate-and-fire model may be necessary. Additionally, application of our modeling approach to a larger CV model might reveal features of the BR sub-system with importance in maintaining homeostasis. We hypothesize that overshoot, adaptation and recovery, features of the BR firing in response the extremes of pressure waves, are critical for regulation of blood pressure during stressful situations, such as a head-up-tilt experiment.

Acknowledgments

Mahdi and Olufsen were partially supported by the VPR project under NIH-NIGMS grant #1P50GM094503-01A0 sub-award to NCSU. Olufsen and Ottesen were supported in part by Snedkermester Sophus Jacobsen and wife Astrid Jacobsens foundation, and Olufsen partially supported by NSF-DMS under awards #1022688 and #1122424. Finally, we would like to thank Alison Margolskee for drawing Figure 1.

References

1. Kardos A, Rudas J Simon, Gingl Z, Csanady M (1997) Effect of postural changes on arterial baroreflex sensitivity assessed by the spontaneous sequence method and valsalva manoeuvre in healthy subjects. Clinical Autonomic Research 7: 143–148.

2. Boron W, Boulpaep E (2005) Medical physiology: A cellular and molecular approach. Philadelphia, PA: Elsevier.

3. Guyton A, Hall J (2006) Guyton and Hall Textbook of Medical Physiology (11th ed.). Philadelphia: Elsevier Saunders.

4. Cowley AJ (1992) Long-term control of arterial blood pressure. Physiological Reviews 72: 231–300.

5. Ketch T, Biaggioni I, RM R, Robertson D (2002) Four faces of baroreflex failure. hypertensive crisis, volatile hypertension, orthostatic tachycardia, and malignant vagotonia. Circulation 105: 2518–2523.

6. La Rovere M, Bigger JJ, Marcus F, Mortara A, Schwartz P (1998) Baroreflex sensitivity and heart-rate variability in prediction of total cardiac mortality after myocardial infarction. Lancet 351: 478–484.

7. Ottesen J (2011) The mathematical microscope making the inaccessible accessible. BetaSys - Systems Biology 2: 97–118.

8. Landgren S (1952) On the excitation mechanism of the carotid baroreceptors. Acta Physiol Scand 26: 1–34.

9. Spickler J, P K (1967) Dynamic response characteristics of carotid sinus baroreceptors. American Journal of Physiology 212: 472–476.

10. Srinivasan R, Nudelman H (1972) Modeling carotid sinus baroreceptor. Biophysical Journal 12: 1171–1182.

11. Srinivasan R, Nudelman H (1972) Theoretical studies on behavior of carotid sinus baroreceptors. Kybernetik 13: 144–150.

12. Ottesen J (1983) Nonlinearity of baroreceptor nerves. Sur Mat Ind 7: 187–201.

13. Alfrey K (1997) Model of the Aortic Baroreceptor in Rat. MS thesis. Houston: Rice University.

14. Chen F, Zhang Y, Zhang C (2004) An integrate-and-fire based baroreceptor model. IEEE/EMBS International Summer School on Medical Devices and Biosensors .

15. Ursino M (1999) A mathematical model of the carotid baroregulation in pulsating conditions. IEEE Trans Biomed Eng 46: 382–392.

16. Lazzaro J, James S, Rogers W (1991) Silicon baroreceptors: Modeling cardiovascular pressure transduction in analog vlsi. In Sequin, C (ed), Advanced Research in VLSI, Proceedings of the 1991 Santa Cruz Conference .

17. Zerbst E, Dittberner KH, Kötter V (1970) Studies on blood-pressure regulation by the use of a baroreceptor analog. Pflügers Archiv 6: 232–249.

18. Itani T, Koushanpour E (1989) A mathematical model of the arterial baroreceptors. In proceeding of: Engineering in Medicine and Biology Society, 1989 Images of the Twenty-First Century .

19. Levison W, Barnett G, Jackson W (1966) Nonlinear analysis of the baroreceptor reflex system. Circ Res 18: 673–682.

20. Brown A, Saum W, Yasui S (1978) Baroreceptor dynamics and their relationship to afferent fiber type and hypertension. Circ Res 42: 694–702.

21. Bronk D, Stella G (1932) Afferent impulses in the carotid sinus nerve i. the relation of the discharge from single end organs to arterial blood pressure. J Cell Comp Physiol 1: 113–130.

22. Bronk D, Stella G (1935) The response to steady state pressure of single end organs in the isolated carotid sinus. American Journal of Physiology 110.

23. Coleridge H, Coleridge J, Kaufman M, Dangel A (1981) Operational sensitivity and acute resetting of aortic barorecetpors in dogs. Circ Res 48: 676–684.

24. Dorward P, Andresen M, Burke S, Oliver J, Komer P (1982) Rapid resetting of the aortic baroreceptors in the rabbit and its implications for short–term and longer term reflex control. Circ Res 50: 428–439.

25. Krieger E, Salgado H, Michelini L (1982) Resetting in baroreceptors. Int Rev Physiol 26: 119–146.

26. Andresen M (1984) Short–and long-term determinants of baroreceptor function in aged normotensive and spontaneously hypertensive rats. Circ Res 54: 750–759.

27. Seagard J, van Brederode J, Dean F, Hopp F, Gallenberg L, et al. (1990) Firing characteristics of single-fibre carotid sinus baroreceptors. Circ Res 66: 1499–1509.

28. Alfrey K (2000) Characterizing the Afferent Limb of the Baroreflex. Ph.D. thesis. Houston: Rice University.

29. Brown A (1980) Receptors under pressure. an update on baroreceptors. Circ Res 42: 694–702.

30. Brown A, Saum W, Tuley F (1976) A comparison of aortic baroreceptor discharge in normotensive and spontaneously hypertensive rats. Circ Res 39: 488–496.

31. Franz G (2007) Nonlinear rate sensitivity of the carotid sinus reflex as a consequence of static and dynamic nonlinearities in baroreceptor behavior. NY Acad Sci 156: 811–824.

32. Saum W, Brown A, Tuley F (1976) An electrogenic sodium pump and baroreceptor function in normotensive and spontaneously hypertensive rats. Circ Res 39: 497–505.

33. Wang W, Chen J, Zucker I (1991) Postexcitatory depression of baroreceptors in dogs with experimental heart failure. Am J Physiol 260: H1160–5.

34. Katona P, Barnett G (1969) Central origin of asymmetry in the carotid sinus reflex. Ann N Y Acad Sci 156: 779.

35. Angell-James J (1971) The responses of aortic arch and right subclavian baroreceptors to changes of non-pulsatile pressure and their modification by hypothermia. J Physiol (Lond) 214: 201–223.

36. Angell-James J (1973) Characteristics of single aortic and right subclavian baroreceptor fiber activity in rabbits with chronic renal hypertension. Circ Res 32: 149–161.

37. Pelletier C, Clement D, Shepherd J (1972) Comparison of afferent activity of canine aortic and sinus nerves. Circ Res 7: 557–568.

38. Warner H (1958) The frequency-dependent nature of blood pressure regulation by the carotid sinus studied with an electric analog. Circ Res 6: 35–40.

39. Franz G, Acher A, Ito C (1971) Small signal characteristis of carotid sinus baroreceptors of rabbits. Journal of Applied Physiology 30: 527-535.

40. Coleridge H, Coleridge J, , Schultz H (1987) Characteristics of c fibre baroreceptors in the carotid sinus of dogs. J Physiol 394: 291–313.

41. Van Vliet B, West N (1987) Response characteristics of pulmocutaneous arterial baroreceptors in the toad, bufo marinus. J Physiol 388: 55–70.

42. Sokolove P, Cooke I (1971) Inhibition of impulse activity in a sensory neuron by an electrogenic pump. J Gen Physiol 57: 125–63.

43. Sherwood L (2001) Human physiology: from cells to systems. Brooks Cole.

44. Wagner H, Humphrey J (2011) Differential passive and active biaxial mechanical behaviors of muscular and elastic arteries: basilar versus common carotid. J Biomech Eng 133: 051009.

45. Kalita P, Schaefer R (2008) Mechanical models of artery wall. Arch Comput Methods Eng 15: 1–36.

46. Valdez-Jasso D, Bia D, Zocalo Y, Armentano R, Banks H, et al. (2009) Viscoelastic models for passive arterial wall dynamics. Adv Appl Math Mech 1: 151–165.

47. Buehler M (2006) Nature designs tough collagen: Explaining the nanostructure of collagen fibrils. PNAS 103: 12285–12290.

48. Fratzl P (2008) Collagen: Structure and Mechanics. New York: Springer Verlag.

49. Fung Y (1993) Biomechanics: Mechanical Properties of Living Tissues. New York: Springer Verlag.

50. Valdez-Jasso D (2010) Modeling and Identification of Vascular Biomechanical Properties in Large Arteries. Ph.D. NCSU.

51. Nekouzadeh A, Pryse K, Elson E, Genin G (2007) A simplified approach to quasi-linear viscoelastic modeling. J Biomech 40: 3070–3078.

52. Yoo L, Kim H, Gupta V, Demer J (2009) Quasilinear viscoelastic behavior of bovine extraocular muscle tissue. Invest Ophthalmol Vis Sci 50: :3721–3728.

53. Fung Y (1996) Biomechanics: Circulation. New York: Springer Verlag.

54. Krauhs J (1979) Structure of rat aortic baroreceptors and their relationship to connective tissue. J Neurocytol 8: 401–414.

55. McDonald D (1983) Morphology of the rat carotid sinus nerve. i. course, connections, dimensions and ultrastructure. J Neurocytol 12: 345–372.

56. McDonald D (1983) Morphology of the rat carotid sinus nerve. ii. number and size of axons. J Neurocytol 12: 373–392.

57. Glazebrook P, Schilling W, Kunze D (2005) Trpc channels as signal transducers. Pflugers Arch 451: 125–130.

58. Drummond H, Price M, Welsh M, Abboud F (1998) A molecular component of the arterial baroreceptor mechanotransducer. Neuron 21: 1435–1441.

59. Bugenhagen S, Cowley AJ, Beard D (2010) Baroreceptor dynamics and their relationship to afferent fiber type and hypertension. Physiological Genomics 42: 23–41.

60. Houk J, Cornew R, Stark L (1966) A model of adaptation in amphibian spindle receptors. J Theoretical Biol 12: 196–215.

61. Hasan Z (1983) A model of spindle afferent response to muscle stretch. Journal of Neurophysiology 49: 989–1006.

62. Taher M, Cecchini A, Allen M, Gobran S, Gorman R, et al. (1988) Baroreceptor responses derived from a fundamental. Annals of Biomedical Engineering 16: 429–443.

63. Lapicque L (1907) Recherches quantitatives sur lexcitation electrique des nerfs traitee comme une polarization. J Physiol Pathol Gen 9: 620–635.

64. Abbott L (1999) Lapicque's introduction of the integrate-and-fire model neuron (1907). Brain Res Bull 50: 303–304.

65. Koch C, Segev I, editors (1998) Methods in neuronal modeling : from synapses to networks. Computational neuroscience, second edition. Cambridge, Mass. MIT Press.

66. Izhikevich E (2007) Dynamical Systems in Neuroscience. The geometry of Excitability and Bursting. Cambridge, MA: MIT press.

67. Schild JH, Clark JW, Hay M, Mendelowitz D, Andresen MC, et al. (1994) A- and c-type rat nodose sensory neurons: model interpretations of dynamic discharge characteristics. J Neurophysiol 71: 2338-58.

68. Miao H, Xia X, Perelson A, Wu H (2011) On identifiability of nonlinear ODE models and applications in viral dynamics. SIAM Rev 53: 3–39.

69. Olufsen M, Ottesen J (2012) A practical approach to parameter estimation applied to model predicting heart rate regulation. J Math Biol, to appear .

70. Kelley C (1999) Iterative Methods for Optimization. Philadelphia, PA: SIAM.

71. Ellwein L, Tran H, Zapata C, Novak V, Olufsen M (2008) Sensitivity analysis and model assessment: Mathematical models for arterial blood flow and blood pressure. J Cardiovasc Eng 8: 94–108.

72. Eslami M (1994) Theory of Sensitivity in Dynamic Systems: an Introduction. Berlin, Germany: Springer Verlag.

73. Frank P (1978) Introduction to Sensitivity Theory. New York, NY: Academic Press.

74. Pope S, Ellwein L, Zapata C, Novak V, Kelley C, et al. (2009) Estimation and identification of parameters in a lumped cerebrovascular model. Math Biosci Eng 6: 93–115.

75. Ipsen I, Kelley C, Pope S (2011) Rank-deficient nonlinear least squares problems and subset selection. SIAM J Numer Anal 49: 1244–1266.

76. Burth M, Verghese G, Valerez-Reyes M (1999) Subset selection for improved parameter estimation in online identification of a synchronous generator. IEEE Trans Power Systems 14: 218–25.

77. Itani T, Koushanpour E (1962) The use of the electroic digital computer to determine best fit of blood volume formulas. J Nuclear Med : 94–99.

78. Bezie Y, Lamaziere J, Laurent S, Challande P, Cunha R, et al. (1998) Fibronectin expression and aortic wall elastic modulus in spontaneously hypertensive rats. Arterioscler Thromb Vasc Biol 18: 1027–1034.

79. Feng B, Li B, Nauman E, Schild J (2007) Theoretical and electrophysiological evidence for axial loading about aortic baroreceptor nerve terminals in rats. Am J Physiol Heart Circ Physiol 293: H3659–H3672.

80. Scher A, Young AC (1963) Servo-analysis of carotid sinus reflex effects on peripheral resistance. Circ Res 12: 152–162.

81. Ottoson D, Shepherd G (1965) Receptor potentials and impulse generation in the isolated spindle during controlled extension. Cold Spring Harbor Symposia on Quantitative Biology New York .

82. Haslach H Jr (2005) Nonlinear viscoelastic, thermodynamically consistent, models for biological soft tissue. Biomechan Model Mechanobiol : 172–189.

83. Mahdi A, Ottesen J, Olufsen M (2012) Qualitative aspects of a novel baroreceptor model. Proc Int Workshop on Innovative Simul for Health Care Backfrieder, Bruzzone, Longo, Novak, Rosen, Eds.: 89-94.

Table 3. The state variables and parameters of the BR models.

Variable	Definition		Units	
p	aortic blood pressure		mmHg	
ϵ_w	aortic wall strain		unitless	
ϵ_1	nerve ending coupling strain 1		unitless	
ϵ_2	nerve ending coupling strain 2		unitless	
ϵ_3	nerve ending coupling strain 3		unitless	
ϵ_{ne}	nerve ending strain		unitless	
f	firing rate		Hz	

Parameter	Definition	Value	Units	Reference
r_0	zero pressure radius	1.13	mm	[79]
h	wall thickness	0.17	mm	[79]
E	elastic modulus	1050	mmHg/mm	[78]
k_{wall}	aortic distensibility	$r_0/(Eh)$	unitless	[26]
τ_a	viscous relaxation constant	0.03	s	[46]
τ_b	viscous relaxation constant	0.01	s	[46]
A_0	unstressed aortic area	3.1414	mm^2	[46]
A_m	maximal aortic area	15.708	mm^2	[46]
α	saturation pressure	145	mmHg	[46]
k	steepness const	5	unitless	[46]
E_0	elastic nerve const	1	mmHg/mm	[59]
E_1	elastic nerve const	1	mmHg/mm	[59]
E_2	elastic nerve const	5	mmHg/mm	[59]
E_3	elastic nerve const	10	mmHg/mm	[59]
η_1	viscous nerve coupling const	2	mmHg/mm	[59]
η_2	viscous nerve coupling const	2.5	mmHg/mm	[59]
η_3	viscous nerve coupling const	1	mmHg/mm	[59]
α_1	nerve ending const	E_0/η_1	unitless	[83]
α_2	nerve ending const	E_0/η_2	unitless	[83]
α_3	nerve ending const	E_0/η_3	unitless	[83]
β_1	nerve ending relaxation rate	E_1/η_1	s^{-1}	[83]
β_2	nerve ending relaxation rate	E_2/η_2	s^{-1}	[83]
β_3	nerve ending relaxation rate	E_3/η_3	s^{-1}	[83]
s_1	firing constant	480	s^{-1}	
s_2	firing constant	100	s^{-1}	
$\bar{s}_1$	firing constant	7.2386	pA	
$\bar{s}_2$	firing constant	1559.7	pA	
g_{leak}	membrane conductance	0.04	μS	[67]
C_m	membrane capacitance	37.5	pF	[67]
V_{th}	voltage threshold	12.5	mV	[67]
t_{ref}	refractory period	0.01	s	[66, 67]

The models considered in this work and defined in Table 2 contain between three and six state variables listed here. Additionally, the parameters for the whole family of BR models together with their nominal values, units and literature references are provided.

Table 4. Optimized values of parameters for the linear models of BR response.

	Data	k_{wall}	α_1	α_2	α_3	β_1	β_2	β_3	s_1	s_2	p_1	p_2	θ	$\mathbf{R^2}$	**RMSE**
$W_eV_1N_a$ IC	sine	0.0063	0.5			0.5			480	100	6.45	46.75			
$W_eV_1N_a$ opt	sine	0.0063	0.5			0.5			1076	375	6.44	46.84		**0.949**	**2.522**
$W_eV_2N_a$ IC	sine	0.0063	0.5	0.4		0.5	2		480	100	6.45	46.75			
$W_eV_2N_a$ opt	sine	0.0063	0.5	0.4		0.5	2		1105	346	6.44	46.89		**0.950**	**2.507**
$W_eV_3N_a$ IC	sine	0.0063	0.5	0.4	1	0.5	2	10	480	100	6.45	46.75			
$W_eV_3N_a$ opt	sine	0.0063	0.5	0.4	1	0.5	2	10	1221	333	6.44	46.95		**0.951**	**2.495**
$W_eV_1N_a$ IC		0.0063	0.5			0.5			480	100					
$W_eV_1N_a$ opt	step 1	0.0063	0.522			0.395			360	104			1.090	**0.899**	**1.860**
$W_eV_1N_a$ opt	step 2	0.0063	0.273			0.407			340	140			1.025	**0.919**	**2.677**
$W_eV_1N_a$ opt	step 3	0.0063	0.241			0.438			378	169			1.025	**0.969**	**2.420**
$W_eV_1N_a$ opt	step 4	0.0063	0.273			0.865			398	201			1.055	**0.983**	**1.832**
$W_eV_2N_a$ IC		0.0063	0.5	0.4		0.5	2		480	100			1		
$W_eV_2N_a$ opt	step 1	0.0063	0.398	0.4		0.310	2		376	102			1.097	**0.905**	**1.800**
$W_eV_2N_a$ opt	step 2	0.0063	0.188	0.4		0.304	2		365	137			1.027	**0.917**	**2.702**
$W_eV_2N_a$ opt	step 3	0.0063	0.132	0.4		0.271	2		480	163			1.099	**0.970**	**2.390**
$W_eV_2N_a$ opt	step 4	0.0063	0.101	0.4		0.552	2		480	201			1.057	**0.983**	**1.823**
$W_eV_3N_a$ IC		0.0063	0.5	0.4	1	0.5	2	10	480	100			1		
$W_eV_3N_a$ opt	step 1	0.0063	0.415	0.4	1	0.303	2	10	404	102			1.100	**0.908**	**1.779**
$W_eV_3N_a$ opt	step 2	0.0063	0.208	0.4	1	0.305	2	10	397	138			1.030	**0.917**	**2.719**
$W_eV_3N_a$ opt	step 3	0.0063	0.135	0.4	1	0.257	2	10	429	163			1.103	**0.970**	**2.426**
$W_eV_3N_a$ opt	step 4	0.0063	0.101	0.4	1	0.523	2	10	429	201			1.060	**0.984**	**1.810**

For the three linear models $W_eV_1N_a$, $W_eV_2N_a$ and $W_eV_3N_a$ of BR response we present the initial and optimized values of their parameters. We used the BR firing data published by Brown [20] for two different stimuli: the sinusoidal-like pressure profile, and step pressure increase with different magnitude.

Table 5. Optimized nonlinear models of BR response: wall strain models

	k_{wall}	A_0	A_m	α	k	α_1	α_2	β_1	β_2	s_1	s_2	τ_a	τ_b	p_1	p_2	$\mathbf{R^2}$	**RMSE**
$W_eV_2N_a$ IC	0.0063					0.5	0.4	0.5	2	480	100			6.46	46.75		
$W_eV_2N_a$ opt	0.0063					0.5	0.4	0.5	2	1105	346			6.44	46.89	**0.950**	**2.507**
$W_{ve}V_2N_a$ IC	0.0063					0.5	0.4	0.5	2	480	100	0.030	0.01	6.46	46.75		
$W_{ve}V_2N_a$ opt	0.0063					0.5	0.4	0.5	2	1112	349	0.028	0.01	6.44	46.77	**0.950**	**2.517**
$W_{ne}V_2N_a$ IC		1	3	150	10	0.5		0.5		480	100			6.46	46.75		
$W_{ne}V_2N_a$ opt		1	32.6	150	10	0.5		0.5		619	109			6.44	46.89	**0.952**	**2.458**

For the three models, $W_eV_2N_a$, $W_{ve}V_2N_a$, and $W_{ne}V_2N_a$, of BR response, we present the initial and optimized values of their parameters. We used the BR firing data published by Brown [20] for a sinusoidal-like pressure profile.

Table 6. Optimized linear and nonlinear models of BR response: Post-excitatory depression.

	k_{wall}		α_1	α_2	β_1	β_2	s_1	s_2	δ_u	δ_d			$\mathbf{R^2}$	**RMSE**
$W_eV_2N_a$ IC	0.0063		0.5	0.4	0.5	2	480	100	4.60	8.70				
$W_eV_2N_a$ opt	0.0063		0.5	0.4	0.5	2	1076	375	4.59	8.59			**0.862**	**7.384**
$W_{ne}V_2N_a$ IC	0.0063		0.5	0.4	0.5	2	480	100	4.60	8.70				
$W_{ne}V_2N_a$ opt	0.0063		0.5	0.4	0.5	2	1076	375	4.59	8.59			**0.883**	**6.795**

	A_0	A_m	α_1	α_2	β_1	β_2	$\bar{s}_1$	$\bar{s}_2$	C	G	V_{th}	t_{ref}	$\mathbf{R^2}$	**RMSE**
$W_{ne}V_2N_{IF}$ IC	3.14	15.71	0.4	0.5	0.5	2	3.40e-10	5.0 e-12	37.5e-11	2.60 e-8	0.00110	0.0070		
$W_{ne}V_2N_{IF}$ opt	3.13	15.71	0.4	0.5	0.5	2	2.947e-10	3.473e-12	37.5e-11	5.019 e-8	0.00116	0.0062	**0.969**	**3.598**

For the three models $W_eV_2N_a$, $W_{ne}V_2N_a$ and $W_{ne}V_2N_{IF}$ of BR response we present the initial and optimized values of their parameters. We used the BR firing data published by Brown [20] for a square pressure profile. For $W_{ne}V_2N_{IF}$ values for $\delta_u, \delta_d, \alpha, \kappa$ were $4.663, 8.788, 145$ and 5 respectively. These are not listed as they were not part of the optimization process for this model.